



DIGITAL ACCESS TO SCHOLARSHIP AT HARVARD

The role of air in droplet impact on a smooth, solid surface

The Harvard community has made this article openly
available.

Please share how this access benefits you. Your story
matters.

Citation	No citation.
Accessed	February 17, 2015 12:22:32 AM EST
Citable Link	http://nrs.harvard.edu/urn-3:HUL.InstRepos:13064817
Terms of Use	This article was downloaded from Harvard University's DASH repository, and is made available under the terms and conditions applicable to Other Posted Material, as set forth at http://nrs.harvard.edu/urn-3:HUL.InstRepos:dash.current.terms-of-use#LAA

(Article begins on next page)

HARVARD UNIVERSITY
Graduate School of Arts and Sciences



DISSERTATION ACCEPTANCE CERTIFICATE

The undersigned, appointed by the

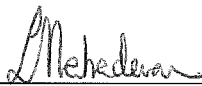
School of Engineering and Applied Sciences

have examined a dissertation entitled

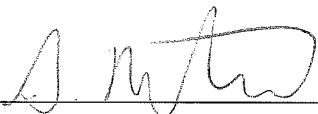
“The role of air in droplet impact on a smooth, solid surface”

presented by : John Kolinski

candidate for the degree of Doctor of Philosophy and here by
certify that it is worthy of acceptance.

Signature 

Typed name: Prof. L. Mahadevan

Signature 

Typed name: Prof. S. Rubinstein

Signature 

Typed name: Professor M. Brenner

Signature 

Typed name: Professor J. Aizenberg

Date: December 6, 2013

The role of air in droplet impact on a smooth, solid surface

A dissertation presented

by

John Kolinski

to

The School of Engineering and Applied Sciences

in partial fulfillment of the requirements

for the degree of

Doctor of Philosophy

in the subject of

Applied Physics

Harvard University

Cambridge, Massachusetts

December 2013

©2013 - John Kolinski

All rights reserved.

Thesis advisor

Author

Prof. L. Mahadevan

John Kolinski

The role of air in droplet impact on a smooth, solid surface

Abstract

The impact of liquid drops on solid surfaces is a ubiquitous phenomenon in our everyday experience; nevertheless, a general understanding of the dynamics governing droplet impact remains elusive. The impact event is understood within a commonly accepted hydrodynamic picture: impact initiates with a rapid shock and a subsequent ejection of a sheet leading to beautiful splashing patterns. However, this picture ignores the essential role of the air that is trapped between the impacting drop and the surface. We describe a new imaging modality that is sensitive to the behavior right at the surface. We show that a very thin film of air, only a few tens of nanometers thick, remains trapped between the falling drop and the surface as the drop spreads. The thin film of air serves to lubricate the drop enabling the fluid to skate on the air film laterally outward at surprisingly high velocities, consistent with theoretical predictions. We directly visualize the rapid spreading dynamics succeeding the impact of a droplet of fluid on a solid, dry surface. We show that the approach of the spreading liquid toward the surface is unstable, and lift-off of the spreading front away from the surface occurs. Lift-off ensues well before the liquid contacts the surface, in contrast with prevailing paradigm where lift-off of the liquid is contingent on solid-liquid contact and the formation of a viscous boundary layer. We show that when a drop impacts an atomically smooth mica surface, a strikingly stable nanometer thin

Abstract

layer of air remains trapped between the liquid and the solid. This layer occludes the formation of contact, and ultimately causes the complete rebound of the drop.

Contents

Title Page	i
Abstract	iii
Table of Contents	v
Citations to Previously Published Work	vii
Acknowledgments	viii
Dedication	ix
1 Introduction and summary	1
1.1 Droplet impacts	1
1.2 The prevailing paradigm of droplet impact	4
1.3 The influence of air in inertial impact dynamics	7
1.4 Summary of this thesis	12
2 Skating on a film of air: drops impacting on a surface	15
2.1 Experimental methods and summary	16
2.2 Direct observation of the thin film of air	20
2.3 Speeding up by slowing down: the virtual frame technique	22
2.4 Getting to the point: photodiode intensity traces at high impact velocity	27
3 Lift-off instability during the impact of a drop on a solid surface	30
3.1 Initial stages of droplet impact	34
3.2 The lift-off transition and the role of viscosity	35
3.3 Implications of the lift-off transition	38
4 Drops can bounce on perfectly hydrophilic surfaces	42
4.1 The kinematics of the liquid-air interface	46
4.2 Characteristic timescale for rebound	47
4.3 Enhanced dissipation in the thin film of air	50
Bibliography	55

A	Experimental methods and details of the calculated velocity for liquid spreading	61
A.1	TIR Measurement	61
A.2	The Virtual Frame Technique	62
A.3	Photodiode measurement	64
A.4	Mathematical model	69
B	TIR calibration methods	70
B.1	Controlled positioning of an object in the evanescent field	71
B.2	Synchronized measurement of a known trajectory using an alternative measurement modality	71
C	The initiation of contact and the stability of the air film	75
C.1	Structure and hydrodynamics of the thin film of air	76
C.2	Linear stability analysis of thin viscous films	78
C.3	Time duration of air film before initiation of liquid-solid contact	80
C.4	Initiation of contact on atomically smooth mica	83
D	The propagation of liquid-solid contact through thin air	87
D.1	Initiation of liquid-solid contact at a point	88
D.2	Propagation of the contact line along the surface	90
D.3	Characteristic geometry of the propagating contact line	92
D.4	A phenomenological model for the propagating contact line	92

Citations to Previously Published Work

Chapter 2 appeared in Physical Review Letters as:

“Skating on a Film of Air: Drops Impacting on a Surface”, John M. Kolinski, Shmuel M. Rubinstein, Shreyas Mandre, Michael P. Brenner, David A. Weitz and L. Mahadevan Phys. Rev. Lett, **108**, 074503 (2012)

Chapter 3 appeared in Physical Review Letters as:

“Lift-off instability during the impact of a drop on a solid surface”, John M. Kolinski, L. Mahadevan and Shmuel M. Rubinstein Phys. Rev. Lett, **112**, 134501 (2014)

Chapter 4 will has been submitted as:

“Drops can bounce on perfectly hydrophilic surfaces”, John M. Kolinski, L. Mahadevan and Shmuel M. Rubinstein

Acknowledgments

The opportunity to work closely with two phenomenal scientists, L. Mahadevan and Shmuel M. Rubinstein, throughout the course of my PhD has been a true privilege; I am fortunate to have had their unyielding support. Many scientists at Harvard and at the Weizmann Institute have been extremely generous with me, and have educated me through lectures and example; the incomplete list includes Jim Rice, Franz Spaepen, Howard Stone, Michael Brenner, with whom I had the privilege of both taking and teaching AM 201, Shreyas Mandre, Madhav Mani, Dave Weitz, who showed me an example of clear, careful and concise composition, Elisha Moses, and the many lecturers at the summer schools I had the opportunity to attend in Denmark, in Boulder, and at Les Houches. My dear friends and colleagues made life enjoyable as I worked on my thesis, especially Matt Pharr, John Platt, Jeff Thompson, Zhiyan Wei, Madhav Mani, Michael Chemama, Otger Campas, Tobias Schneider, Joerg Fritz, Niall Mangan, Aryesh Mukherjee, Thierry Savin, Mahesh Bandhi, Miriam Huntley, Aaron Mowitz, Omer Gottesman, Francesco Tassinari, Valentina Caracuta and many others. I am grateful for the welcome and support I received at the Weizmann Institute, where I spent over a year as a visiting student in Shmuel's lab. In particular, Sid Cohen, Yael Heyman and Irit Goldian provided an invaluable contribution to this work as we investigated the stability of the thin film of air. The entire community at the Weizmann Institute made my visits a joy; in particular the wonderful international community of students and post-docs. I am deeply grateful for the support and generosity of my family. Finally, I was very fortunate to receive support for my research from the NDSEG fellowship and the NSF GRFP. These fellowships gave me flexibility to learn.

Dedicated to my family and friends

Chapter 1

Introduction and summary

1.1 Droplet impacts

From washing dishes in a sink, to raindrops falling on the windshield as we drive down the highway, droplet impact is ubiquitous in our daily experience. Indeed, droplet impact plays a crucial role in industrial processes, from 3-D printing of scaffolds for the construction of bio-materials[22] to heat transfer[32, 7] to forensic science[1]. Despite its ubiquity, a general understanding of the underlying physical mechanisms governing droplet impact remains elusive. For example, since the pioneering studies of splashing by Worthington[61], many thresholds for determining when a drop will eject daughter drops and splash upon impacting a surface have been proposed[8, 16, 30, 33, 44, 47, 56, 57, 59, 65]; however, several of these thresholds contradict one another[36], and only the most recent threshold accounts for ambient pressure in the surrounding air[65]: indeed, the prevailing paradigm used in modeling the impact of liquid drops on solid surfaces completely ignored the surrounding air[6].

Thus, droplet impact constitutes a subtle and challenging problem in interfacial fluid mechanics, and significant questions about drop impact dynamics remain open.

Several recent experimental studies provide a glimpse into the important role played by air during the impact of a liquid drop on a smooth surface[48, 65, 49, 14, 13, 19, 54]. These experimental studies are complemented by a variety of analytical techniques[27] and simulations[26, 25] that have lead to predictions about the influence of the air at the earliest stages of the impact event. Theoretical modeling predicts the presence of a nanometer thin film of air beneath the impacting drop[26], and this nanometer thin film of air is directly observed in experiments[19]. The influence of the air at the highest impact velocities is disputed[13, 19]; however, measurements conducted at the shortest timescales provide experimental support for the prediction[26] that the air mediates droplet impact dynamics at even the highest impact velocities[19].

The general phenomenology of droplet impact is not solely comprised of splashing; indeed, depending on parameters of the drop, the surface and the gas, many impact outcomes are observed[40, 66, 36]; several of these outcomes are shown in Fig. 1.1. Just as the air affects the splashing phenomenon, the air also enables this rich variety behaviors upon impact.

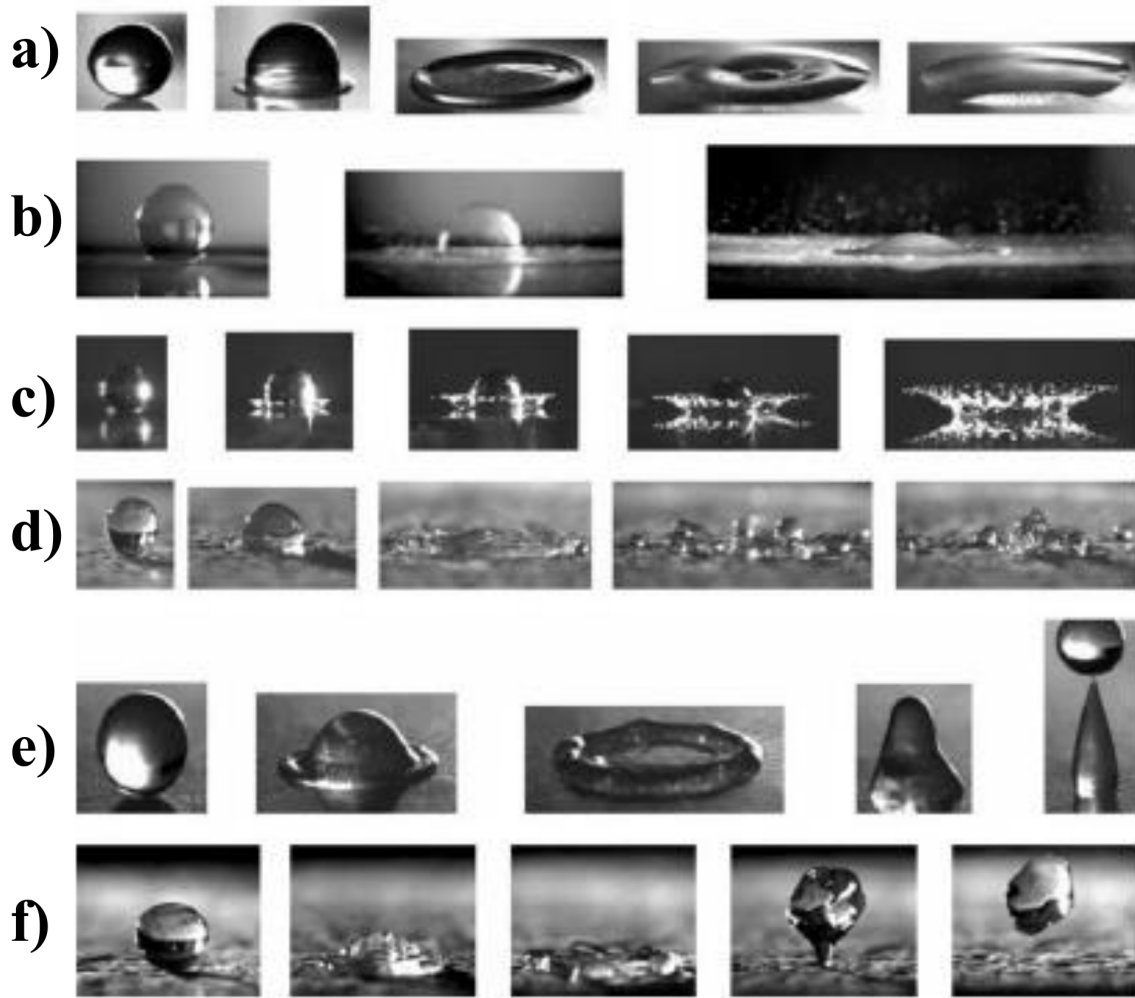


Figure 1.1: Outcomes of droplet impact. From Rioboo et. al. (2001). Courtesy of Begell House. (a) At low V , a drop will spread over a smooth surface. (b) High V impact on a rough surface results in a prompt splash. (c) A corona splash occurs when a drop impacts on a smooth surface with a sufficiently high velocity. (d) High V impact on a superhydrophobic surface results in receding break-up. (e) Partial rebound occurs for impact upon a smooth, hydrophobic surface. (f) Complete rebound occurs from a superhydrophobic surface.

1.2 The prevailing paradigm of droplet impact

1.2.1 The initial stage of droplet impact

At impact velocities significantly lower than those required for a splash but not significantly lower than 1 m/sec, the prevailing paradigm for droplet impact ignores liquid viscosity at the earliest stages[29, 35]; the assumption that viscosity is negligible at the earliest stages of the impact event is supported by a high Reynolds number $Re = RV/\nu$. For typical a 1 mm-radius drop of water falling at $V = 1$ m/sec, $Re \sim 1000$. Observation of the initial stages of liquid solid contact beneath a drop approaching a surface at a slow rate show very rapid dynamics, as can be seen in Fig. 1.2(a). These rapid dynamics suggest that the liquid viscosity can be neglected in the mathematical model used to describe the propagating contact line[3]; indeed, the initial spreading stage of a spherical drop is well-described by a balance of liquid inertia and the surface tension as[10]:

$$\rho \left(\frac{r}{t}\right)^2 = \frac{\gamma}{z(r) \sim r^2},$$

and the spreading front follows the scaling behavior $r \sim (R\gamma/\rho)^{1/4}t^{1/2}$, as can be seen in Fig. 1.2 (b). Notably, there are no studies of the short-time viscous dynamics during the wetting of a solid surface by a liquid drop[4].

1.2.2 Compressible liquid droplet impact paradigm

Until the last decade, theory and experiment suggested that splashing was predicted upon the detachment of a liquid shockwave from the propagating contact line[24, 23] as illustrated in Fig. 1.3; however, the critical jetting angle predicted

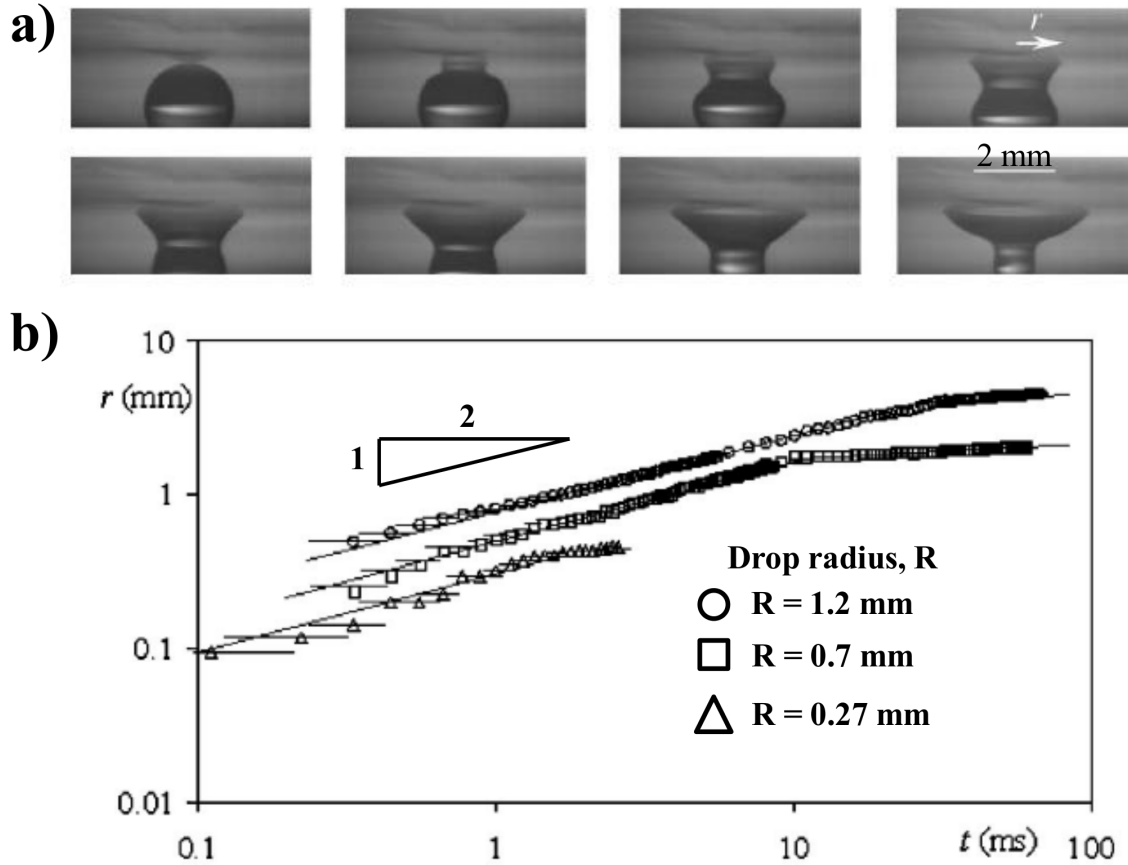


Figure 1.2: Spreading of a liquid drop following the initiation of contact with the surface. Adapted from Biance et. al. (2004). Courtesy of APS. (a) A time series of images recording the initial spreading stages of a mm-scale liquid drop along a wetting glass surface after initiating contact from a quasi-static approach to the surface. Images are separated by ~ 1 msec, and the scalebar in the last image is 2 mm. (b) The spreading radius r is plotted as a function of time for three different drop radii corresponding to the three symbols. Here, we observe that the initial spreading stages spread as $r \sim t^{1/2}$, and then abruptly transition to a ‘Tanner’s law’ regime, where $r \sim t^{1/10}$.

by theory significantly underestimated the jetting angle observed in experiment[35], suggesting that the liquid shockwave model was an incomplete description of the splashing dynamics. The shockwave was assumed to originate at the stress singularity formed when the drop initially contacted the surface at a point centered upon the impacting axis. Since the air is significantly less dense and less viscous than the liquid, it was ignored in these initial models of droplet impact; thus, there was no other means of regularizing the stress singularity caused by the initial impact at a point. Therefore, any finite impact velocity resulted in a diverging compressive stress at the leading edge of the impacting drop, and shocks were expected to emanate through the liquid at even the lowest regime of impact velocities[35], where the liquid Mach number for a water drop moving at 1 m/sec is approximately 0.001, which suggests that the liquid is not sufficiently compressible to generate a shock. While it is possible that many of the results from investigations into compressible liquid impacts apply for liquid Mach numbers exceeding 1, these results have been extended into the low impact velocity regime[35], where other effects such as air compression are now understood to intervene before a shock can be generated in the liquid drop[26, 27, 25].



Figure 1.3: Detachment of a shockwave in the liquid from the solid surface, and consequent ejection of the splash at the base of the drop. From Lesser and Field (1983). Courtesy Annual Reviews Inc.

1.3 The influence of air in inertial impact dynamics

1.3.1 Experimental evidence of the influence of the air on drop impact dynamics

As described above, the prevailing paradigm for droplet impact did not take the air into account. Recent experiments using high-speed imaging show that indeed, the liquid drop does not make contact with the surface on the impact axis as had been assumed in this classical paradigm[24, 35]. Rather, the drop is deformed by the air into a non-convex geometry preceding impact[48, 65, 49, 14, 13, 19, 54]; thus, the stress singularity is resolved in the air before liquid-solid contact initiates. In a typical impact event contact initiates at the boundary of this dimple; as a result, a bubble of air is trapped in the liquid[48, 49]. However, the most striking demonstration of the importance of air in the impact process is the suppression of the splashing

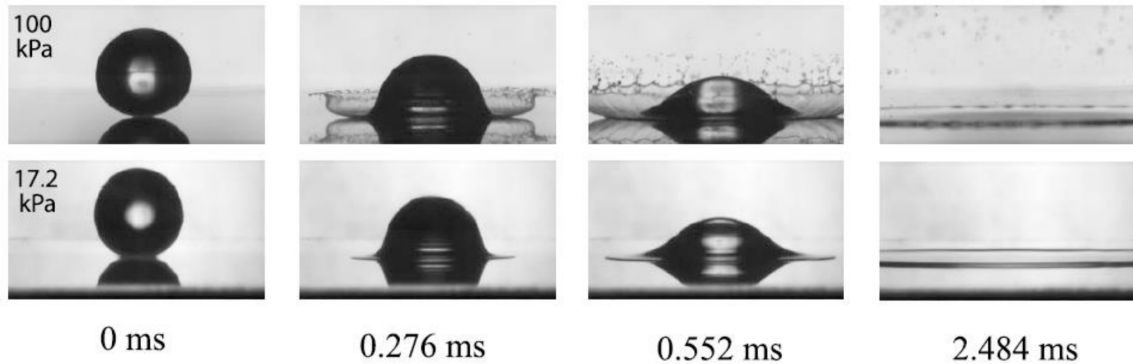


Figure 1.4: Impact of a drop under different ambient pressure and associated collapse of splashing threshold data. From Xu et. al. (2005). At ambient pressure, a mm-scale drop will emit a sheet when impacting with sufficient velocity, as can be seen in the top row of images. When the air pressure is slightly reduced, the same drop will deposit on the surface, as can be seen in the bottom row of images.

phenomenon with a reduction in ambient pressure, as shown in Fig. 1.4[65]. While a critical ratio of stresses in the gas and stresses restraining the liquid was suggested to define the threshold for splashing or not for the highest velocity impacts studied[65], the underlying mechanism for the splash remained an open puzzle.

1.3.2 Seeking a mechanism: simulations of the impact of an inviscid drop falling through a viscous, compressible gas

In order to provide a mechanism for the splashing phenomenon, the impact process was simulated[26] and the moments preceding impact were analyzed[27]. The simulation included both the viscosity and compressibility of the gas, which had not been included in prior studies of liquid drop impact on solid surfaces. The liquid was modeled as an inviscid fluid. The simulation showed two fundamental regimes

in the approach dynamics: first, the droplet inertia is balanced by gas compression, leading to the invagination of the dimple on the underside of the drop; next, diverging curvatures at the rim of the dimple precipitate a transition to a regime where gas compression balances surface tension. As the dimple is forming, the air cannot escape from the thin gap beneath the drop instantaneously, but is instead compressed by the liquid. The relevant height scale at which the drop begins to deform is estimated using a balance of the pressure required to decelerate the liquid drop $\rho_l V^2 \sqrt{R/H}$ with the lubrication pressure in the gas $\mu_g V R/H^2$:

$$H^* = RSt^{2/3},$$

where $St = \mu_g/\rho_l VR$ [26]. For mm-scale drops impacting with a velocity $V = 1.5$ m/sec, just above the splashing threshold, $H^* \sim 1\mu\text{m}$. Therefore, the relevant impact timescale is $H^*/V \sim 2/3\mu\text{sec}$, in good agreement with the simulations, as shown in Fig. 1.5(a). Thus, the dynamics of droplet impact occur at diminutive length scales and fleeting timescales.

As the drop proceeds toward the surface, the underside of the drop begins to flatten. Within a fraction of a microsecond, the drop suddenly changes from a convex, spherical geometry into a non-convex, incurvate shape. At the periphery of the dimple, the liquid continues to funnel out away from the impact axis, and toward the surface, where it approaches more and more closely. As the curvature at the periphery of the dimple begins to steepen, the second regime of the approach dynamics takes over. Asymptotic analysis[26, 27] suggests a transition from a balance of liquid inertia and gas compression to a balance of surface tension and gas compression; this is predicted to occur within 100 nm or closer of the surface. The expression resulting

from the asymptotic analysis of the liquid interaction with the gas predicts that the liquid will approach no closer than $h_{min} \sim 5\delta^{2/3}$; the exact pre-factor is provided by the numerical solution, and dimensionally, $h_{min} \approx 5R\delta^{2/3}St^{2/3}$; thus for a 1 mm drop of water impacting at 1.5 m/sec, the liquid approaches no closer than $h_{min} \approx 30 \text{ nm}^1$. Snapshots from the simulations used to calculate the fluid deformation as the liquid approaches the surface at this diminutive distance are shown in Fig. 1.5(b). At this distance from the surface, interfacial forces could conceivably play a role in the impact dynamics[62]; however, the simulation does not incorporate a model for liquid-solid contact[26].

1.3.3 Direct measurement of the liquid-air interface during the impact event

The simulation and model predict that the liquid skates over a thin film of air more thin than the mean-free-path of air at room temperature and pressure[26]. In the absence of experimental support, this prediction can be disputed. Thus, experimental studies of the initial moments before the drop contacts the surface are required to test whether the liquid skates over such a thin film of air.

An interferometry technique was used to directly visualize the liquid-air interface during the impact event. Using this technique, the formation of a trapped bubble of air was observed, but no significant air layer persisted beneath the drop as the splash occurred[13].

¹The similarity solution ignores the role played by liquid viscosity. Our results, particularly those of Ch. 3, suggest that liquid viscosity is important even at the earliest stages of the impact event; therefore, viscous effects could affect this similarity solution

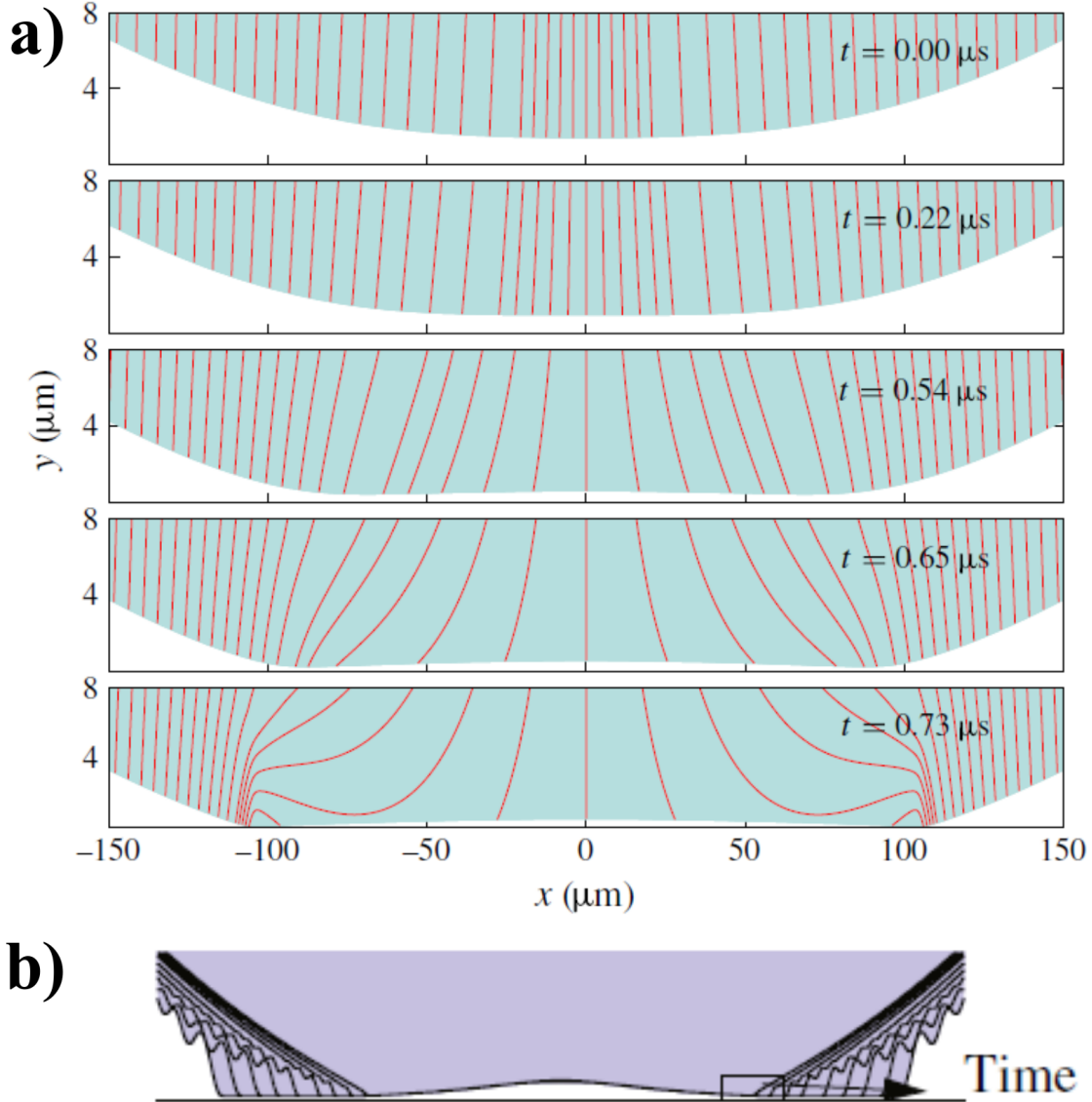


Figure 1.5: Simulation of the approach of an inviscid drop through a compressible, viscous gas film. From Mandre and Brenner (2011). (a) Snapshots from a simulation as the liquid droplet approaches within 10s of nm from the surface. The snapshots show the rapid development of the dimple as the drop transitions from a convex sphere to an incurvate shape. (b) As the curvature diverges at the rim of the dimple, the liquid transitions to skating over a thin film of air supported by a balance of surface tension with the gas pressure, and capillary waves are emitted.

Independently, a TIR technique² was used to probe the liquid air interface directly[19]. The TIR method showed that low-velocity impacts (below the splashing threshold) unequivocally skate on a thin film of air, of order nanometers thick, as the drop deforms and flows over the surface; however, this study shows that the air layer can very rapidly break down beneath the spreading drop with dynamics reminiscent of spinodal decomposition of thin viscous films[58, 62, 37], as shown in Fig. 1.6(a). The dynamics of the breakdown of the air film suggest that as the thickness of the air decreases, the air film will break down more and more rapidly, as shown in Fig. 1.6(b). These observations suggest that the liquid skates over a thin film of air, but that the film of air breaks down rapidly behind the spreading front.

1.4 Summary of this thesis

1.4.1 Ch2: Skating on a film of air

Theoretical predictions of the nanometer-thin film of air demanded a new form of measurement capable of resolving sub-optical, diminutive length scales, and fleeting timescales. In order to resolve these scales, we adapt a TIR microscopy technique, previously used to directly image a frictional interface at the onset sliding friction[42], to directly image the liquid-air interface as the drop approaches within nanometers of the surface.

²For supporting material describing the TIR technique, see App. A and App. B

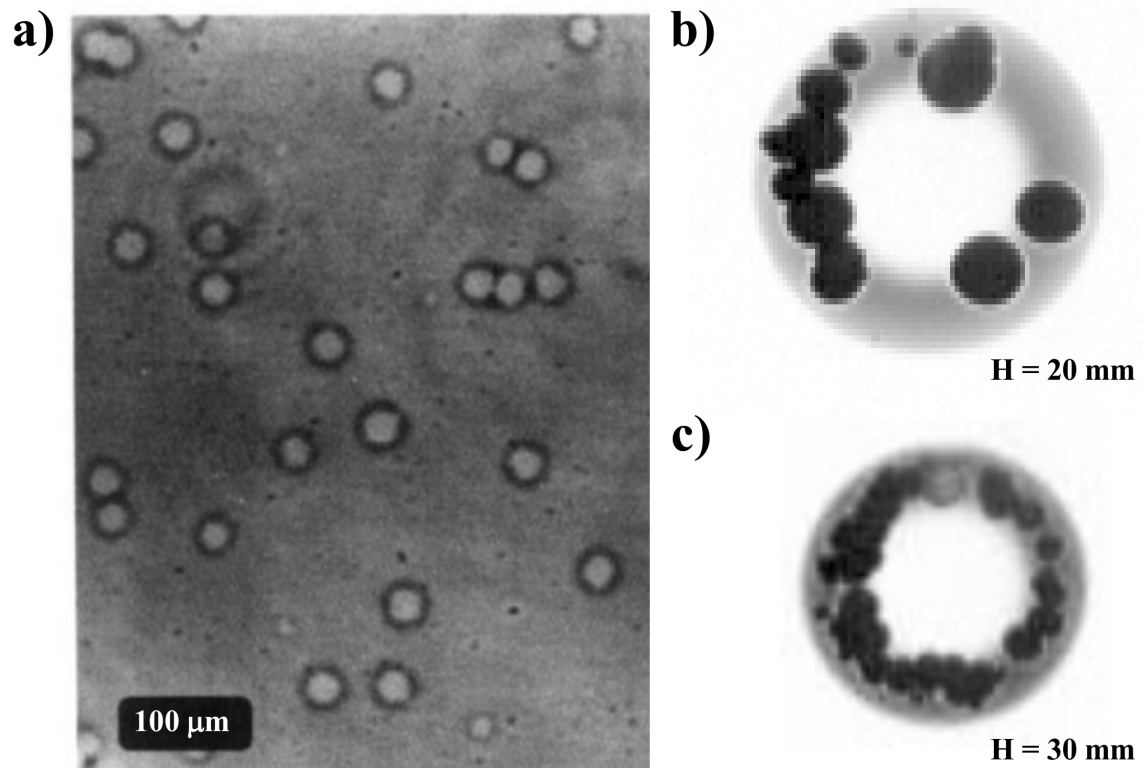


Figure 1.6: Dissolution of thin viscous films. (a) from Reiter (1992) and (b) from Kolinski (2012). (a) Thin polystyrene films coating a silicone wafer will spontaneously form holes; these dynamics result from spinodal dewetting of the polystyrene film from the surface. (b) Thin films of gas beneath an impacting drop of IPA falling from $H = 2$ cm (top) and $H = 3$ cm (bottom) demonstrate dynamics reminiscent of those from (a); indeed, as the film of air beneath the impacting drop forms closer and closer to the surface, the number of contacts increases, the spacing between contacts decreases, and the rate of contact formation increases, in qualitative agreement with the dynamics anticipated from a linear stability analysis of thin viscous films.

1.4.2 Ch3: Lift-off transition in viscous drop impact

Previous studies of the effect of liquid viscosity on splashing[14] had shown that sheet ejection is both delayed and flatter for more viscous liquids; however, liquid viscosity is neglected in mathematical models of droplet impact. We directly probe the liquid air interface using the TIR microscopy technique, and show that in the initial stages of the impact dynamics, the liquid will suddenly transition from piercing through the air toward the surface, and lift-off away from the surface at a viscosity-dependent timescale. The lift-off transition is delayed and flatter for more viscous liquids, similar to the trends observed for higher velocity impacts that result in a splash[14].

1.4.3 Ch4: Rebound from a mica surface

We study the impact of a liquid drop on an atomically smooth, hydrophilic mica surface. For impact on the mica, the air layer is stable down to single-nm thicknesses, resulting in complete rebound from the surface. Droplet rebound had been observed from superhydrophobic surfaces[38, 39], but liquid-solid contact occurs on the surface texture; for rebound from the mica surface, the liquid does not touch the solid. Indeed, rebound from the mica surface is less vigorous than rebound from superhydrophobic surfaces because of the shear in the nm-scale film of air.

Chapter 2

Skating on a film of air: drops impacting on a surface

Raindrops splashing on a car window, inkjets printing on a sheet of paper and the dripping faucet in the kitchen, are all everyday experiences which depend on the impact of drops of fluid on a surface. As familiar as these phenomena are, the impact of a drop of fluid on a surface is, in fact, quite complex [27, 66, 10, 45, 4]. Particularly stunning are the beautiful splashing patterns that often occur [60, 18]; our understanding of these is predicated on very rapid impact followed by a shockwave as the fluid bounces back from the surface [23, 24]. However, before contact can occur, the drop must first drain the air separating it from the surface. Indeed, experimental studies showing the suppression of splashing at reduced ambient pressure underscore the importance of the air [65, 14, 35, 27, 26]. Recent theoretical calculations suggest that, even at moderate impact velocities, the air fails to drain and is instead compressed, deforming and flattening the bottom of the drop while serving

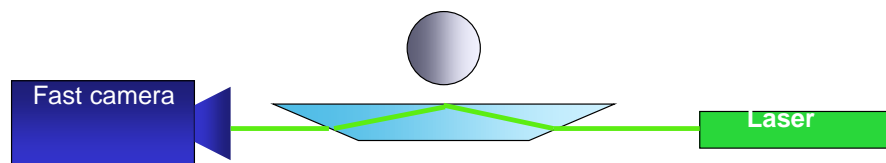
as a thin cushion of air a few tens of nanometers thick to lubricate the spread of the drop [27, 26], and leading to the eventual formation of a trapped bubble of air within the drop [49]. However, the initial stages of impact occur over diminutive length scales and fleeting time scales, and the very existence of this thin film of air remains controversial[13]; indeed, this film has never been directly observed. Moreover, the mechanisms leading the breakup of this film and the ultimate wetting of the surface have never even been considered. Testing these ideas requires direct observations of the impacting interface; however, this demands development of new experimental methods to attain the requisite spatial and temporal resolution.

2.1 Experimental methods and summary

In this letter, we describe direct measurements of the initial contact dynamics of a drop impacting a dry glass surface. To visualize the impact we image from below rather than from the side; to discern the very thin film we combine total internal reflection (TIR) microscopy[42] with a novel virtual frame technique (VFT). We directly observe a thin film of air that initially separates the liquid from the surface enabling much more rapid lateral spreading of the drop providing striking confirmation of the theoretical predictions [27]. However, we also observe a complex sequence of events that leads to the rupture of the film and ultimate contact of the liquid with the solid surface; the initially smooth air film breaks-up as discrete holes are formed and are filled by the liquid. These holes rapidly spread and coalesce into a ring of wet surface surrounding a trapped bubble of air.

To observe the thin film of air, we illuminate the top surface of an optically

a



b

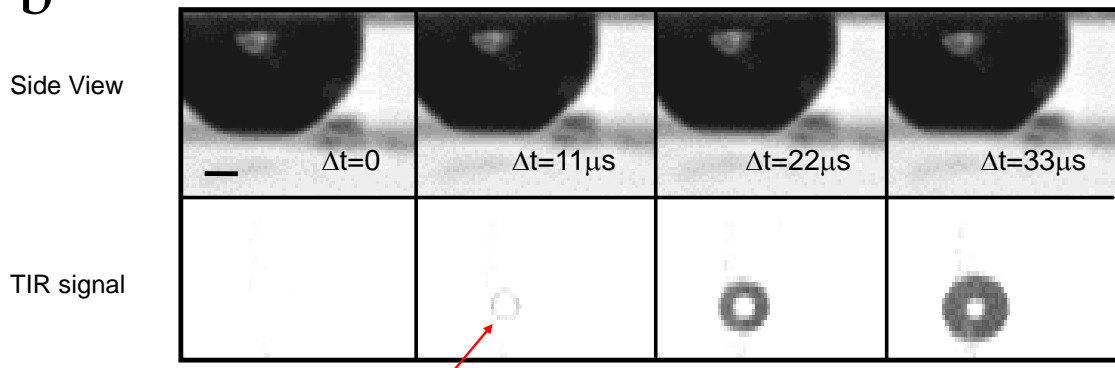


Figure 2.1: : Experimental setup. (a) Schematic of TIR microscopy. (b) Four typical images of a 2.6-mm-diameter drop, falling from $H = 21\text{cm}$ viewed simultaneously from the side and with TIR. Scale bar is $400\mu\text{m}$

smooth dove prism (BK7 glass) with collimated light incident from below at an angle greater than the critical angle for total internal reflection at a glass-air interface but smaller than that at the glass-liquid interface. The reflected light is imaged with a fast camera, as shown schematically in Fig. 2.1a. The light reflected from each point of the interface, $I_r(x, y)$, depends exponentially on the separation between the impacting fluid and the solid surface, with a characteristic decay length that depends on the angle of incidence and is of order of 100nm; as the separation decreases further of the incident light is no longer fully totally internally reflecting and I_r decreases. This directly probes the thin film of air. We illustrate this using a 1.3-mm-radius isopropanol (IPA) drop falling from an initial height $H = 21\text{cm}$. Where H is the distance from the surface to the tip of the nozzle where the drop is generated. When the drop is far from the surface the illuminating beam is totally internally reflected and nothing is observed as shown in Fig. 2.1b; we thus define the last frame before we observe a change in the image as $t = 0$. However, as the separation between the drop and the solid surface becomes comparable to decay length of the evanescent field some of the incident light is no longer totally internally reflected and I_r decreases; thus, a faint ring is observed as the impact dynamics begin, at $t = 11 \mu\text{s}$. In this case the fluid is not actually wetting the surface; instead the drop is supported by a thin layer of air. When wetting finally occurs, there is no longer any totally internally reflected light and a dark ring is observed, at $t = 22\mu\text{s}$. As the drop continues to impinge on the surface the ring of wetting fluid grows both in the outward and inward directions, as shown for $t = 33\mu\text{s}$.

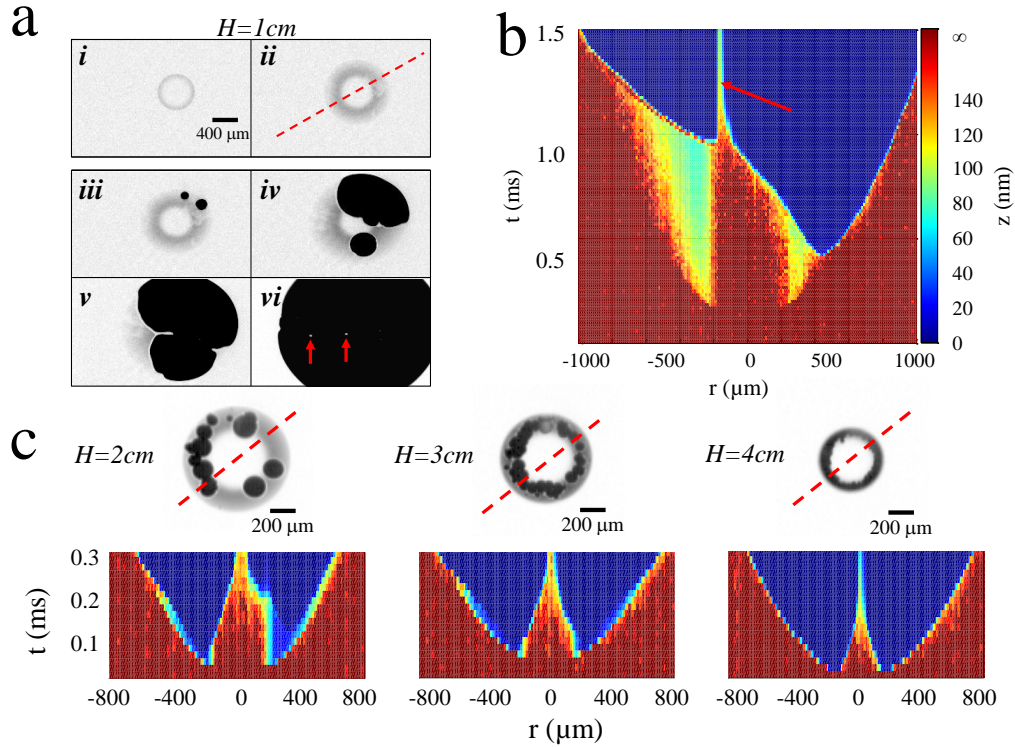


Figure 2.2: The behavior of the thin air film separating the impacting drop from the surface. (a) Six TIR snapshots of a drop, released from $H = 1\text{ cm}$ illustrating the film of air and the impact dynamics. The two bubbles remaining in the drop are indicated by the arrows in vi. (b) The impact dynamics along the cut shown by the dashed line in (a ii). The height is indicated by the color. Arrow indicated one of the bubbles that remains trapped in the liquid (c) The TIR images and time evolution of the air films along the dashed lines for $H = 2, 3$ and 4 cm . The exposure time for all snapshots was $5\ \mu\text{s}$

2.2 Direct observation of the thin film of air

To elucidate the impact dynamics we explore the behavior of drops falling from different initial heights. For $H = 1\text{cm}$, we first detect the drop when a thin ring appears with an inner diameter of about $500\ \mu\text{m}$, as shown in Fig. 2a.i. The outer dimension of the ring grows rapidly as the drop falls, with an outwards velocity of $\sim 1\ \text{m/s}$, comparable to the impact velocity of $0.44\ \text{m/s}$, as shown in Fig. 2.2a.ii. However, the fluid does not actually contact the surface; instead, the fluid spreads on a film of air only $\sim 100\ \text{nm}$ thick. To visualize the dynamics we take a cut through the image at the location shown by the dashed red line in Fig. 2.2a.ii, convert the measured intensity to separation and plot the time evolution, using colour to denote the height, as shown in the 2D graph in Fig. 2.2b. The first $500\ \mu\text{s}$ clearly show the formation of the layer of air as the drop spreads before the liquid contacts the surface. The liquid does not spread inwards, as seen by the boundaries of the thin film, denoted by the central red region; this reflects the pocket of air which ultimately becomes a bubble trapped in the drop.

While the layer of air is clearly responsible for decelerating the drop, it cannot retain the separation of the fluid and surface indefinitely; ultimately, the thin film of air becomes unstable and contact occurs¹. Initially, two small dark spots appear in the film when the liquid fully contacts the surface, as shown in Fig. 2.2a.iii. These are denoted by the dark blue region at $t \sim 0.8\text{ms}$ in Fig. 2.2b. As these spots grow, other spots appear, as the film of air breaks down, as shown in Fig. 2.2a.iv. These liquid wetting fronts spread rapidly, wetting the surface at a velocity of 1.5m/s , comparable

¹The dynamics of the propagating contact line are discussed in detail in App. D

to that of the liquid spreading on the thin film of air. Interestingly, there is a thin line of air at the front of the spreading fluid where the air film becomes thicker as the air is pushed by the advancing wetting front, as shown by the white region leading the edge of the black wetting front. Ultimately two small air bubbles remain, displaced from the center of the drop, as shown by the arrows in Fig. 2.2a.vi and Fig. 2.2b.

Similar dynamics persist as the initial height of the drop is increased: the drop is again decelerated by a thin annulus of air with a thicker pocket in the middle; however, the thickness of the film of air also decreases, becoming of order 10nm for a drop height of 4cm. As H increases the initial size of the inner air pocket also decreases; moreover, the time during which its size remains constant is also reduced. Similarly, the thin film of air is only clearly observed over a much smaller region, prior to complete contact. For example, for $H = 3\text{cm}$, the air film is $\sim 20\text{ nm}$ thick and is already only partly observed at the outer edges of the annulus, as shown by the 2D graph and confirmed by the snapshot (Fig. 2.2c). As we increase the initial drop height to 4cm, contact appears to occur around the full ring more rapidly than our frame rate of 60 kHz; however, even here the initial wetting is discontinuous, occurring in numerous discrete points as indicated by the rough texture of the inside of the ring. Thus, the drop is decelerated by an even thinner film which then breaks up at discrete locations. As we increase H above 4cm, we no longer have sufficient temporal resolution to routinely observe the initial film of air as it exists for a time that is short compared to the inter-frame time of the camera. Serendipitously, on rare occasions, the timing is exactly right that the camera captures the air film during the $1\ \mu\text{s}$ exposure time even at H as high as 21 cm, confirming the existence of the air

film at these larger heights.

2.3 Speeding up by slowing down: the virtual frame technique

To overcome this inherent limitation imposed by even the highest speed camera, we introduce a new imaging method, exploiting the fact that the intensity will change from completely bright to completely dark for a very small change in the liquid-solid separation. We exploit this nearly binary contrast by increasing the camera exposure time to integrate over times longer than the characteristic dynamics. This is illustrated schematically for a wetting front moving in one dimension in Fig. 2.3a, using a composite image, which reflects the sum of the individual images at each time. The over-exposed image displays a linear black to white gradient; this is essentially the sum of a series of individual virtual frames, which can be recovered by taking consecutive thresholds. We therefore call this method the virtual frame technique (VFT). The temporal resolution is determined by the dynamic range of the camera; thus, using a camera with 14-bit dynamic range, and an exposure time of $100 \mu\text{s}$ the VFT would allow us to resolve dynamics as short as 6 ns! For specific imaging sensors[15], this temporal resolution can be further improved by exploiting the gamma correction, which provides the camera an optional nonlinear integration time, and is particularly useful for isolating dynamics of accelerating fronts. Moreover, with VFT, the full spatial resolution of the camera is preserved. Thus, the VFT provides a combination of spatial and temporal resolution that is much greater than for any

camera available (see App. A).

We employ the VFT to study the impact dynamics of drops released from initial heights ranging from 1cm to 50cm. For all H , the integrated image is disk shaped with a darker ring where contact first occurs, a bright white spot in the middle where the air bubble remains, and an evolution from black to gray to white moving outwards where wetting has not yet occurred, as shown in Fig. 2.3b. For $H = 2\text{cm}$ there are pronounced features in the image which are not observed for larger values of H , where the images are more symmetric. These features reflect the non-uniform nature of the initial wetting, consistent with the images in Fig 2.2c.

To quantify the VFT data, we measure intensity as a function of radial distance along the dashed line shown in Fig. 2.3b, and plot the results in the inset of Fig. 2.3c. The intensity data are converted to time to obtain the temporal evolution of the front, which is shown for several values of H in Fig. 2.3c. The lower branch of each curve reflects the inward-traveling front as the ring closes to entrap the bubble in the middle of the drop; the upper branch of each curve reflects the outward-traveling front as the falling drop spreads. The point where the two meet is the radial distance at which contact first occurs, R_0 ; this is a decreasing function of initial height, as shown in Fig. 2.4a, and the radial contact disc size exhibits a power-law dependence on H , with an exponent of $1/6$, consistent with theoretical predictions[27] (see also App. A), as shown in the inset.

To explore the initial dynamics of the wetting associated with the rupture or break down of the air cushion, we numerically calculate the local instantaneous velocity and plot its magnitude as a function of radial position, r . The inward-moving velocity

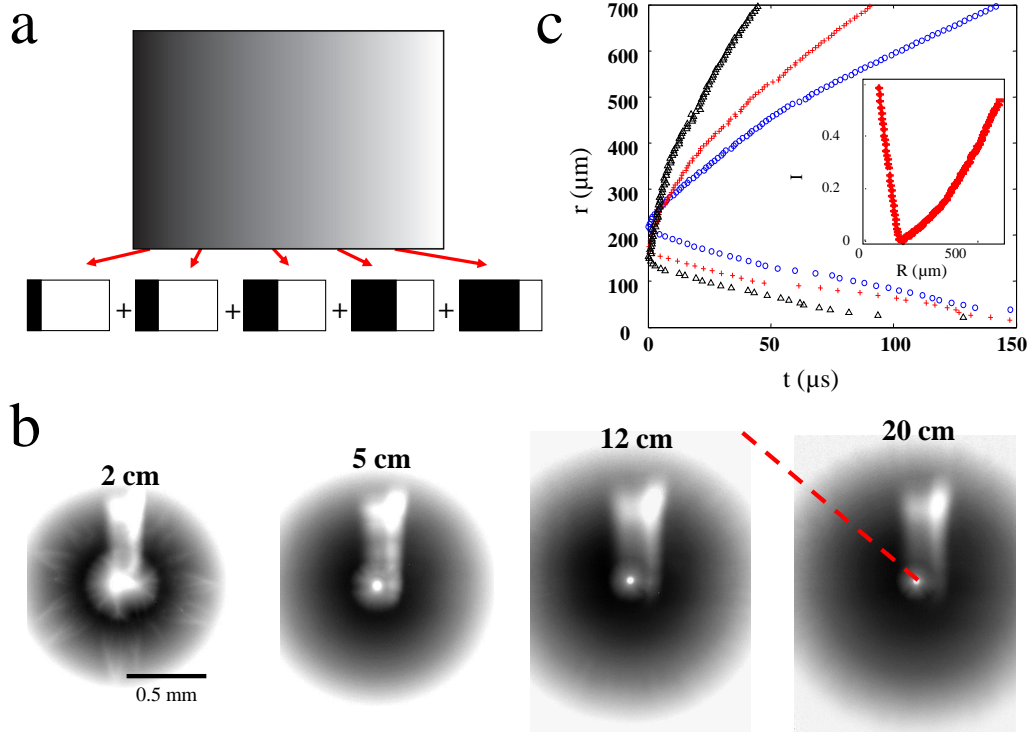


Figure 2.3: Virtual Frame Technique (VFT). (a) 1D schematic demonstrating the concept. Individual binary images, below, are integrated to yield the total gray-scale image. The gray scale can be interpreted to yield the time evolution. (b) Four VFT images taken different values of H . Each image exhibits a square-shaped whiter region through the top center resulting from spurious reflections in the beam path; they are ignored in our analysis. (c) The intensity is converted to time and azimuthally averaged around the impact center. The distance of the wetting fronts from the center are plotted as a function of time for three typical experiments with $H = 26, 126, 456$ mm for blue circles, red pluses and black triangles respectively.

is constant, propagating at approximately 1.3 m/s; by contrast, the outward-moving velocity decreases as $1/r$, and can exhibit remarkably high values, as large as ~ 70 m/s, as shown in Fig. 2.4b. Surprisingly, the velocity of the inward-moving front is independent of H ; by contrast the maximum velocity of the outward-moving front increases strongly with H , as shown in Fig. 2.4c. Moreover, the maximum velocity of the outward-moving front is nearly an order of magnitude greater than the capillary velocity for IPA, $\gamma/\mu \approx 10$ m/s.

When a contact line advances, it must flow on very small scales to maintain contact with the interface; flow on these small scales is dominated by viscous dissipation and thus, the propagation rates are limited by the liquid capillary velocity. By contrast, the velocities measured here are much larger; this suggests that the fluid is not in contact with the surface but is instead spreading on a thin film of air; thus, the very early viscous dissipation is in the gas as it is squeezed out from under the liquid that wets the surface at μ . Indeed, such high velocities are predicted theoretically as discussed in App. A, but only with the explicit assumption that the spreading occurs over a film of air, as indicated by the excellent agreement between the calculated behavior, shown by the solid line, and the data in Fig. 2.4c. Although the VFT assumes nearly binary data, the resulting virtual frames will be practically indistinguishable for a simple dry-wet transition and an extremely short lasting air film which is followed immediately by a wetting front.

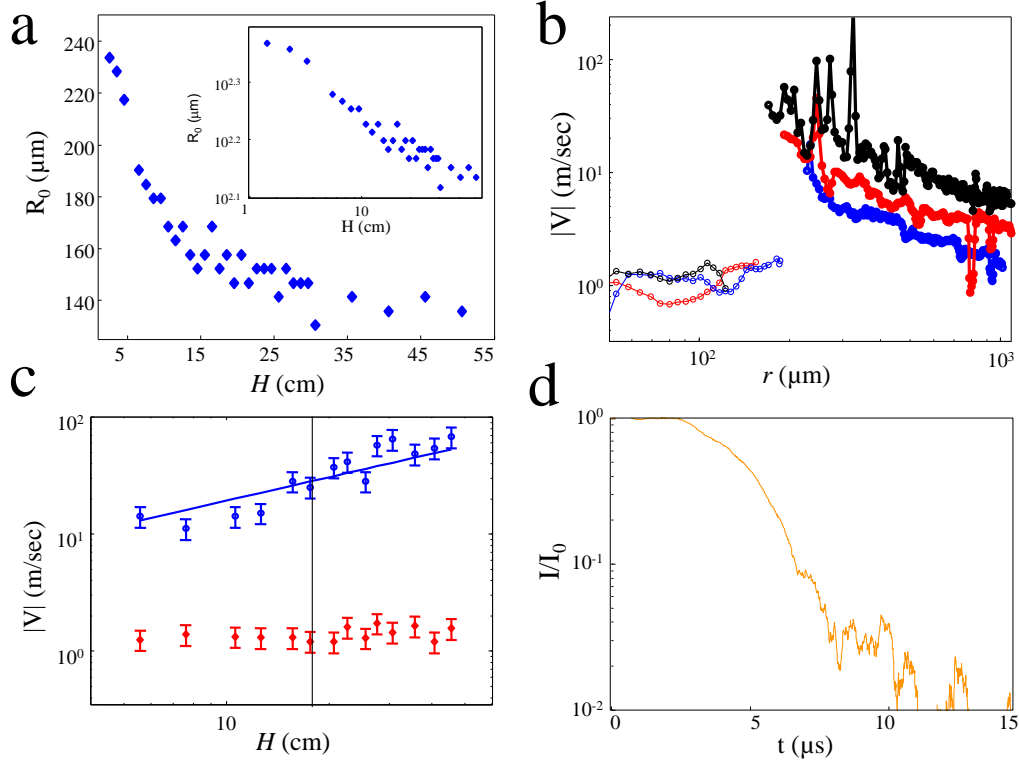


Figure 2.4: The initial dynamics of the wetting. (a) R_0 , as a function of H (inset) same as main figure in log scale. (b) The inwards (solid circles) and outwards (open circles) velocity of the spreading liquid for $H = 26, 126, 456$ mm corresponding to blue, red and black respectively. (c) Peak velocities for the outwards (blue circles) and inwards (red circles) fronts. Blue curve is the theoretically predicted initial outwards spreading velocity, as discussed in App. A. The dashed line indicates the threshold height above which splashing is observed. (d) A photo diode trace acquired at 100MHz measuring the intensity of the reflected light directly underneath the thin air film at a location marked by a red spot in the inset, for $H = 21$ cm. The dashed blue line marks the measurement noise floor. (inset) Close up of the low intensity region. The image shown is a direct visualization of the thin film of air separating the liquid from the surface prior to contact.

2.4 Getting to the point: photodiode intensity traces at high impact velocity

To monitor the thin film of air for $H = 21$ cm, we measure the intensity using a photodiode operating at 100 MHz. The photodiode detects an area $\sim 2500\mu\text{m}^2$; by comparison, the thin film of air is initially about $200\mu\text{m}$ in diameter, as shown by the camera image in the inset to Fig. 2.4d. We normalize the photodiode intensity to that obtained before the drop hits the interface, I_0 . The intensity initially drops rapidly, corresponding to the passage of the liquid over the area sampled by the photodiode; the steep slope of the intensity drop is indicative of the very high speed at which the liquid spreads. However, the intensity does not drop all the way to zero, but instead levels off, reaching a plateau at a value $I/I_0 \sim 0.1$, and finally decreasing to zero after $\sim 5\mu\text{s}$ as shown in the enlarged data in the inset of Fig. 2.4d. This plateau directly reflects the existence of the thin film of air that separates the liquid from the surface. The nature of the final decay of this plateau differs from experiment to experiment, as shown for example in Fig. A.2ii. This reflects the specific dynamics of the dewetting of the air film, which can vary due to the specific spinodal decomposition that occurs in each case. These measurements directly confirm the spreading of the liquid on a thin film of air of order 10 nm thick; this is trailed closely by a wetting front that rapidly expands due to the breakdown of the air film.

Our results directly demonstrate the existence of a thin film of air over which the liquid spreads; this provides striking confirmation of the theoretical prediction[27, 26]. In addition, our results reveal that qualitatively new phenomena occur as the thin film

of air becomes unstable; simultaneously breaking down at many discrete locations, leading to wetting patches that grow and coalesce to fully wet the surface. Similar dynamics have also been reported to occur when a sheet of fluid is ejected as a drops splash after high velocity impact [51, 14]. For a perfectly wetting fluid such as IPA on glass, a thin film of air behaves as does a poor solvent; it cannot remain stable and van der Waals forces will cause it to de-wet the surface through a nucleation or spinodal-like process [37, 11]; indeed Fig. A.2a.ii is reminiscent of the patterns observed in such processes. De-wetting dynamics are traditionally considered to be quite slow [37, 11], however, for spinodal de-wetting the rate of film breakup depends strongly on its thickness[11] and also on viscosity and may occur very rapidly; for example, a 10nm thick air film will remain stable for no longer than one microsecond. Thus, rupturing occurs simultaneously at many discrete locations; this leads to small wetting patches that grow and coalesce to fully cover the surface, thereby very rapidly following the advancing fluid front. This gives the appearance of a single contact line moving at the same velocity as the fluid, much faster than the calculated capillary velocity.

Using a novel experimental modality that visualizes the falling drop from below rather than from the side, we identify a thin film of air that initially separates the liquid from the surface. Eventually, however, spinodal-like dewetting of the air film always leads to its breakup and complete contact of the surface by the fluid. The rate at which contact occurs depends on the rate of this spinodal-like process, which depends on the thickness of the air film. Initially, as H is increased, the air film becomes thinner, and the breakup of the air film occurs more rapidly; thus, even

though the rate of initial drop spreading increases with H , the length over which the drop skates on the air film decreases. However, as H increases still further, the thickness of the air film saturates, and hence the rate of breakup also saturates; however, the rate of initial spreading of the drop continues to increase with H . Thus, the drop always can skate over the film of air, even as H continues to increase. Interestingly, this skating on the film of air can persist, even until H increases enough that a sheet of fluid is ejected near the expanding rim, and a splash is produced. This suggests that dynamics of this ephemeral film of air may be of far greater importance, and may in fact influence splashing; however, confirmation of this speculation requires further investigation.

Chapter 3

Lift-off instability during the impact of a drop on a solid surface

Over a century since the pioneering work of Worthington investigating splashing of liquid drops[60], the dynamics of the interaction between an impacting drop of fluid and the surface it wets has attracted the attention of researchers[60, 23, 24, 41, 20, 65, 66, 12]. When drop impact occurs at moderate velocities, the dynamics are traditionally considered to be quite simple: For a drop that is brought into contact at a slow, quasi static rate, contact initiates at a point centered on the impact axis, then spreads laterally to coat the surface uniformly[3, 4]. The rate at which the contact line spreads is determined by the balance between the inertia of the liquid and the surface tension of the interface[3, 4]. In these regimes, viscosity is negligible in comparison to inertia and surface tension and its effect is therefore ignored[3, 4]. Since the dynamics of this slow approach are governed by inertia, it is customary to sustain this picture when the approach velocity is increased[29, 45].

The quasi static picture, however, completely ignores the role that the surrounding air plays in the impact dynamics. Indeed, before a drop will contact a surface, the separating air must first be drained. Draining the air becomes increasingly more difficult as the gap between the liquid and the solid surface diminishes, up to a time when the air fails to drain and instead compresses, while the bottom surface of the drop is deformed and the liquid spreads laterally outward and not downward. As a result of this process, a small bubble of air remains trapped within the liquid once contact occurs[50, 48, 49, 28, 53]. Indeed, many beautiful experiments have shown over the past few years that the ambient air has a critical role in the dynamics of droplet impact[65, 49, 9, 63, 64, 52, 14, 13, 21, 43, 55, 19, 5].

Perhaps the most striking example for the role of air in the dynamics of impacting drops is the total suppression of splashing when the ambient atmospheric pressure is reduced to a third of an atmosphere[65]. More recently, it was shown, initially theoretically[26, 27] and then experimentally[19], that when a drop impacts a surface the outwards spreading of the liquid can occur over a thin film of air, a few hundreds of nanometers in thickness or even less. The presence of a thin lubricating air layer enables the liquid to spread outward at very high velocities, high enough to support the formation of a singular sheet of liquid at the leading edge. However, the mechanism for the lift-off of the liquid away from the surface that enables splashing at high impact velocities remains elusive. Current theoretical models and calculations require the initiation of full contact between the fluid and solid[25]; this in turn requires the formation of a viscous boundary layer to enable lift-off of the liquid. Experimental testing of these dynamics is challenging and requires ultra-fast measurement of the

nanometer-thin film of air.

In this Letter we explore in detail the fluid dynamics occurring as drops of Newtonian liquids impact on a solid, dry surface. We investigate the rapid spreading of the liquid over a nanometer-thin film of air following the impact of the drop for water-glycerol mixtures and for non-aqueous silicone liquids over a wide range of viscosities. The surface of impact is imaged from below with rapid Total Internal Reflection (TIR) microscopy[19]. We find that the initial spreading velocities of the liquid are largely independent of the viscosity of the liquid. This observation is consistent with theoretical predictions, which showed that the dynamics of drop impact are approximated well by an inviscid liquid[26]. Surprisingly, we also observe a new instability in the profile of the spreading liquid which was not previously observed nor predicted theoretically; the leading edge of the liquid abruptly transitions from an extremely sharp cusp into a curved, rounded profile and the liquid subsequently lifts-off away from the surface. It is interesting that although the spreading rate is independent of the liquid viscosity, the time at which the transition to lift-off occurs relative to the instant of initial impact does depend on viscosity, and scales as the viscosity to the power of one half.

The rapid dynamics occurring directly above the interface are measured with TIR microscopy and a fast camera. TIR is a well-established imaging technique that we recently adapted for fluid dynamics, and which enables us to directly probe with unprecedented high speeds the dynamics of nanometer thin films of air formed beneath the liquid drop. The experimental setup is described elsewhere[19], and is also shown schematically in Fig. 3.1a. A collimated, monochromatic beam of light undergoes

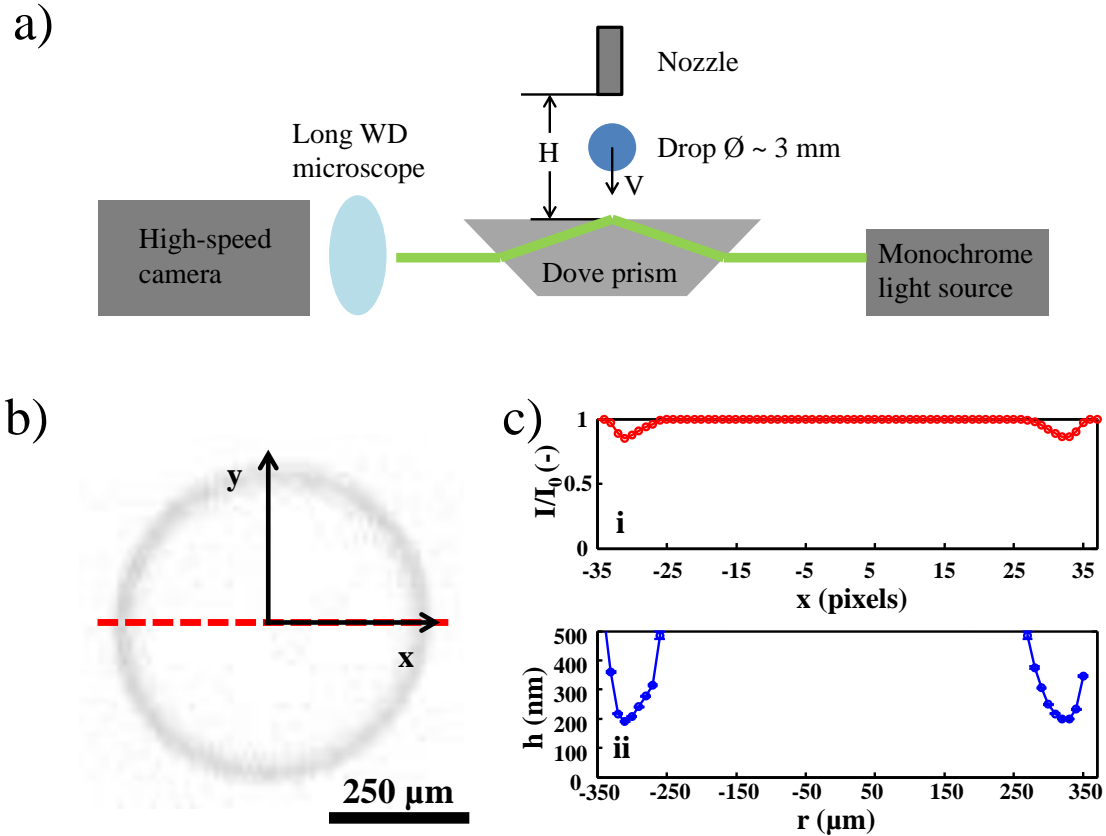


Figure 3.1: TIR-microscopy: (a) Schematic of the experimental setup. H , is the height from the surface to the nozzle from which the drop falls. (b) A typical fast camera snapshot of a liquid-air interface before contact taken approximately 10 microseconds after the dimple has formed. (c) (i) The normalized intensity trace taken along the cut marked by the red dashed line in (b) (ii) The height of the liquid above the solid surface plotted against distance for the same trace shown in (c).

total internal reflection off of the surface of impact, generating an exponentially decaying evanescent field. The angle of incidence of the light on the interface is chosen such that the condition for total internal reflection is maintained for a glass-air interface, but not for the glass-liquid interface. The reflected intensity is imaged with our fast camera's sensor. When a drop of liquid enters the evanescent field, light tunnels through the liquid-air interface and the reflected intensity decreases; this appears as a grayscale on our imaging sensor. The evanescent wave decays over a length scale which is a function of the angle of incidence, and in our experiments is typically 100 nm, allowing us to clearly identify films of air as thin as a few nanometers. The high resolution achieved by TIR allows us to directly observe the thin film of air that initially appears as a gray ring on our imaging sensor, as shown in Fig. 3.1b. We are also able to sharply distinguish between surfaces that are separated from the liquid by a thin film of air and a wet surface, as well as extracting absolute height information by converting the pixel grayscale intensity into height, as shown in Fig. 3.1c.

3.1 Initial stages of droplet impact

To investigate the initial impact dynamics of drops over a large range of parameters, we study drops of different size and surface tension, and vary the viscosity by two orders of magnitude, from 1 to 100 cSt. This is obtained by using both water-glycerol mixtures and silicone oils of various viscosities. We restrict this study to initial (release) heights between 8 mm and 30 mm and image the dynamics at a rate of up to 180,000 frames per second with a fast camera (Phantom V711). Before the liquid contacts the solid, the air beneath the drop flows out but fails to completely drain, and

the bottom surface of the drop deforms as the liquid funnels outwards; this process leads to the formation of a dimple that at later times develops into a trapped bubble of air within the drop[48, 5]. Moreover, after forming the dimple, the liquid does not immediately wet the surface, but instead continues skating rapidly over a nm-thin film of air, as shown for an aqueous drop impacting on a smooth glass surface in Fig. 3.2a. In all of our experiments, we observe the liquid skating over a nm-thin film of air, consistent with previous experiments conducted with a low-viscosity alcohol[19]; moreover, for all the liquids we used, the initiation of liquid-solid contact in each of our experiments occurred similarly to previously observed discrete breakdown of the thin air film. In this letter we restrict our description to the dynamics occurring prior to any wetting.

3.2 The lift-off transition and the role of viscosity

For a given impact velocity, the initial rate at which the liquid spreads over the thin film of air is nearly identical for all the different liquids, in spite of a difference of two orders of magnitude in viscosity. This can be seen by the similar spacing between the time-dependent profiles shown in Fig. 3.2b and c as well as also in the inset to Fig. 3.3b where we plot the instantaneous spreading rates of liquids of different viscosities are compared. In spite of the striking consistency in spreading rates, the spreading dynamics do indeed vary markedly for different viscosities. For all impact parameters measured the leading edge of the liquid initially progresses slightly toward the surface, however, this process is unstable. Instead, a sharp transition is observed, with the liquid abruptly lifting off away from the surface. While for low-viscosity

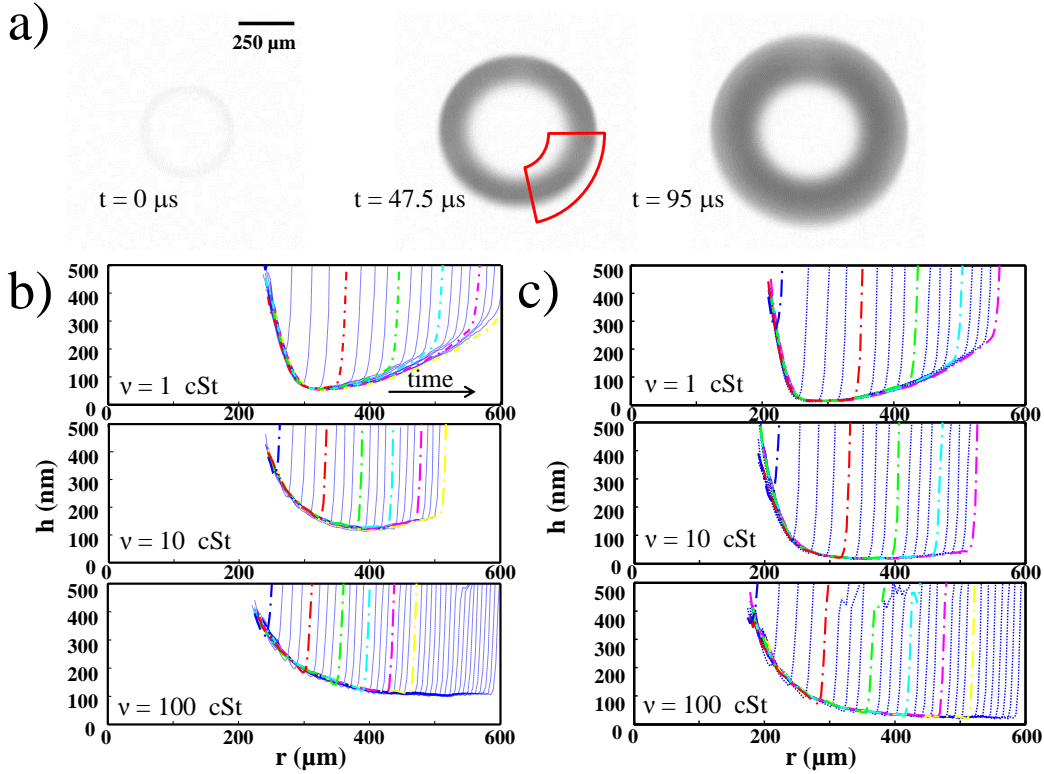


Figure 3.2: : Skating on a thin film of air:(a) three TIR snapshots separated by $45 \mu\text{sec}$ showing the spreading of a 10 cSt water-glycerole mixture over a thin film of air, at an impact speed of 0.54 m/sec. The red semi-annular region in (i) denotes a typical area used to calculate the annular-average profiles shown in (b) and (c). (b) Liquid-air interface profiles for water-glycerol mixtures impacting the solid surface at an average velocity of 0.45 m/sec. The three plots correspond to different liquid viscosities while the different curves within each plot show consecutive time traces, separated by 5 microseconds. Note that although the viscosity differs by up to two orders of magnitude the spreading velocity highlighted by the space of separation between consecutive profiles is practically identical for the different liquids. Similar behavior is observed in (c), where the impacting drops of identical dimensions to those in (b), but the impact velocity is higher, at 0.63 m/sec. For this impact velocity, the asymptotic air film thickness is on average 4 times smaller; nevertheless, for both impact velocities, the dependence of the spreading dynamics on the liquid viscosity is qualitatively similar. Color is used to highlight traces occurring at the same time.

liquids the lift-off occurs almost immediately, for the higher viscosity liquids it is delayed for up to a hundred microseconds during which the liquid spreads to a lateral extent exceeding several hundred microns, as shown in 3.3b and c. In fact, for the 100 cSt liquid, the air layer is already beginning to break down beneath the liquid before we observe a liftoff of the spreading front. Surprisingly, even though the thickness of the thin film of air significantly decreases with impact velocity, all other features of the spreading dynamics are remarkably similar; thus, they depend strongly on the viscosity of the liquid and not significantly on the thickness of the thin film of air beneath the spreading liquid, as shown by comparing the two panels in Fig. 3.3b and c.

We characterize the viscosity dependence of the spreading and lift-off dynamics by examining individual profiles, a typical example for this is shown in Fig. 3.3a. For each experiment, we identify two points on the drop rim profile, one where the liquid is closest to the surface, and whose distance from the impact center is r_m and whose height above the surface is h_m . The second point is where the liquid front exhibits maximal curvature, which is a good measure for the location of the leading edge of the liquid. Its radial distance to the drop impact center is r_c and its height above the surface is h_c . We calculate the rate at which the liquid spreads outward, V_c , by taking the numerical derivative of r_c . The outward spreading of the liquid sets-in as the drop approaches the surface immediately following its deformation by the compressed air; therefore, all the liquid is funneled outward at a velocity that decays as $t^{-1/2}$, as shown in Fig. 3.3b. In the initial stages of impact, the spreading is dominated by the inertia of the drop and the spreading velocity is prominently independent of viscosity,

as shown in the inset to Fig. 3.3b where we compare the instantaneous spreading velocity measured at a normalized time $tV/R = 0.05$, marked by the dashed line in the main figure. The origin of t , t_0 is chosen by estimating the instant that the center of the drop would contact the surface in the absence of air, $t_0 = r_{hmin0}^2/2RV$.

The outward spreading front progresses in a rate independent of liquid viscosity, nevertheless, the dynamics of the lift-off away from the surface do depend strongly on liquid viscosity. For all viscosities the liquid front is initially led by a sharp high curvature cusp and the fastest spreading liquid is closest to the surface; thus, at this stage, $r_m = r_c$. However, after a time τ , that does depend on viscosity, the liquid lifts off away from the surface; thus r_c deviates from r_m and h_c differs from h_m . We define these parting length scales as Δ_r and Δ_h respectively. At time τ , Δ_r and Δ_h sharply increase from zero, as clearly seen for Δ_r in Fig. 3.3c and Δ_h in Fig. 3.3d, respectively. h_m decreases exponentially as shown by the inset in Fig. 3.3d. Surprisingly, before h_m decays to an asymptotic value, r_m stops increasing abruptly; this corresponds to the moment the spreading front begins to lift-off away from the surface. The time, τ measured relatively to the initial entry of the liquid into the evanescent field, at which the fluid motion becomes unstable and begins to lift away from the surface is highlighted by the vertical dashed lines in Fig. 3.3c and d.

3.3 Implications of the lift-off transition

The timescale τ corresponding to the sudden lift-off transition exhibits a scaling of $\nu^{1/2}$, as shown in Fig. 3.4a. Since the velocity of spreading is independent of viscosity, our results indicate that the point of lift-off is significantly farther from the

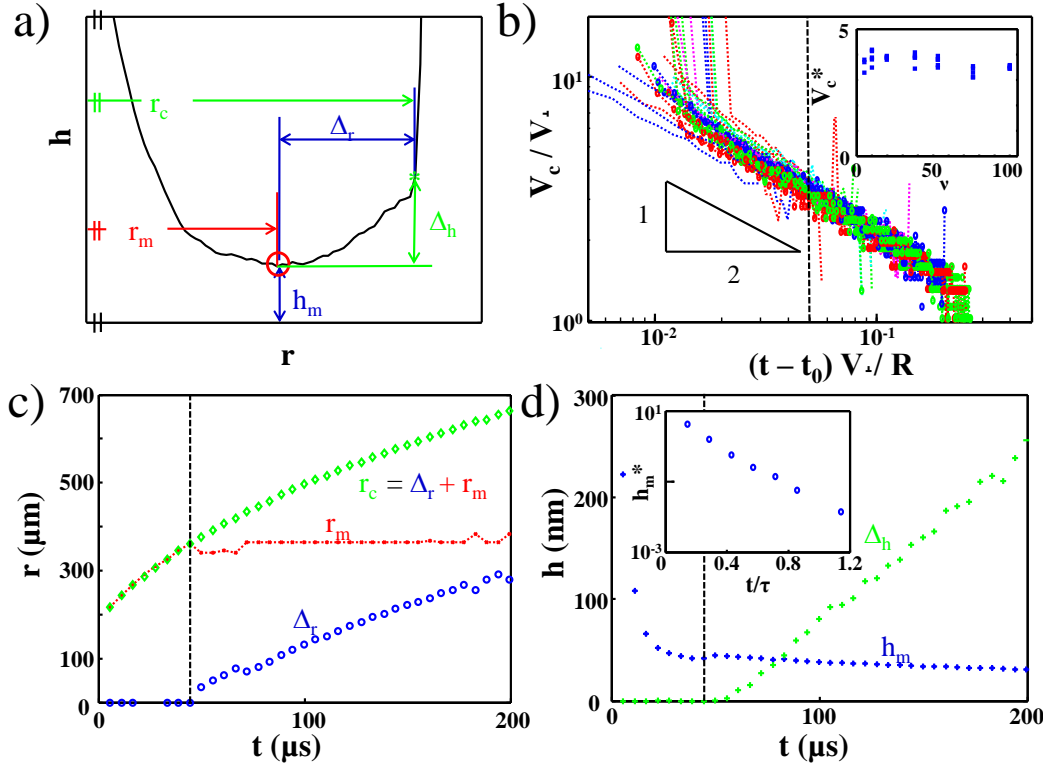


Figure 3.3: : Spreading and lift-off dynamics. (a) Typical example of the profile of a low viscosity liquid spreading over a thin film of air. The point of minimum thickness, (t_m, h_m) , is indicated by a red circle. We identify the leading edge of the spreading liquid, (r_c, h_c) , as the point of maximum curvature and mark its position by a green asterisk. (b) When the spreading velocity parallel to the surface, V_c is normalized by the impact velocity V and then plotted against the dimensionless time normalized by the relevant impact timescale, R/V , we see that all curves collapse to one master curve. The insert shows the instantaneous spreading velocities taken at the time marked by the dashed line in the main figure, $V_c^* = V_c((t - t_0)V_\perp/R) = 0.05$. (c) A typical example of the spreading dynamics $r(t)$ shown for a 10 cSt impacting at 0.64 m/sec. The time τ when the leading edge of the drop r_c begins to differ from the point closest to the surface r_m is precisely where the liquid lifts-off. This is highlighted by the dashed black line. (d) h_m and h_c as a function of time for the same experiment plotted in (c). The insert depicts a semi logarithmic plot of the normalized minimal distance from the surface $h_m^* = (h_m(t) - h_m(\tau))/h_m(\tau)$ plotted as a function of t/τ note that the liquid approaches the surface at an exponential rate.

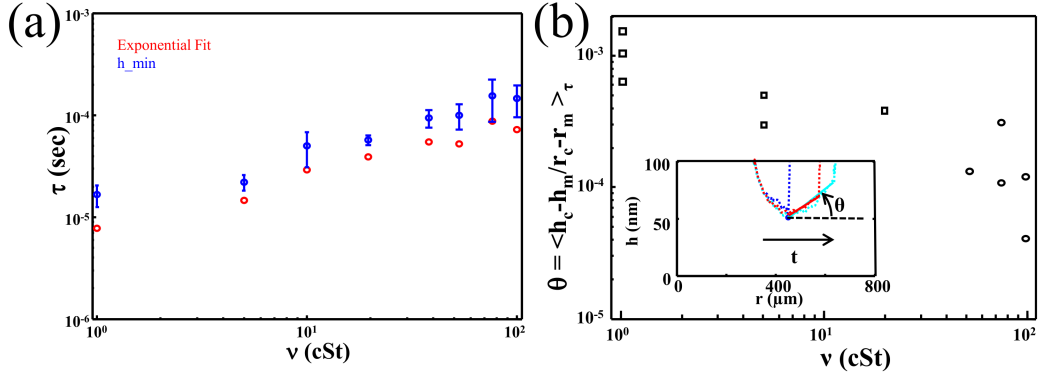


Figure 3.4: Lift-off dynamics: Typical time scale before lift-off, τ , as a function of viscosity, ν , measured in two different ways: extracting a typical timescale from an exponential fit to $h_{min}(t)$ (red) and the first instance $\Delta_r > 0$ (blue). The black line is a $\nu^{1/2}$ and serves as a guide for the eye (b) Lift-off angle, Θ , highlighted in the inset and as a function of ν .

impact center for more viscous fluids compared to less viscous fluids. This is perhaps analogous to recent results showing that viscous drops delay ejection of a sheet during a splash[14]. Moreover, we observe a persistent slope once the liquid begins to lift off away from the surface. The lift-off is much flatter for more viscous drops, as shown by the average slope shown in Fig. 3.4b, which may also be analogous to the flatter corona sheet observed in the viscous splashing experiments [14]. However, those viscous splashing experiments [14] are conducted with considerably higher impact velocities; furthermore, in these and similar experiments, no persistent thin film of air beneath the impacting drop was observed.

Nevertheless, the similarity between the behaviors in these two experimental regimes may suggest that the instability leading to the lift-off of the spreading front is related to the mechanism for the formation and rise of the corona in a viscous splash. However, determining whether or not the novel lift-off instability reported here is directly related to splashing of viscous drops will require future studies of high

speed droplet impact

Chapter 4

Drops can bounce on perfectly hydrophilic surfaces

The impact of liquid droplets on solid surfaces is ubiquitous in many natural and industrial settings. Depending on the impact parameters, a liquid drop may spread uniformly, it may break up into secondary drops and splash or it can even bounce off, detaching away from the surface[66]. While spreading and splashing occur under a wide range of conditions[65, 66, 36, 63, 21], it is traditionally thought that drops will only bounce off of a special solid surface that is superhydrophobic; textured and functionalized to comply with a Cassie-Baxter state, wherein the liquid is supported by micron-sized asperities and the interstitial air[31, 46, 38]. Surprisingly, the important role played by the surrounding air in the dynamics of droplet impact on smooth solid surfaces was only recently explored in experiments[65, 63, 13, 19, 55, 21] and theoretical work[26, 27, 25]. Direct visualization of the impact surface revealed that the impact dynamics are mediated by the formation of a nanometer

thin film of air separating the liquid from the surface[19], consistent with theoretical predictions[26, 27]. It was found that there are two stages to the impact event: first, as a liquid drop approaches the surface, the separating air fails to drain and instead compresses, leading to the formation of a dimple on the bottom surface of the drop[48, 49]. Second, after the formation of the dimple, the liquid rapidly spreads outward, skating over a nanometer-thin film of air[26, 27, 19]. At this stage the liquid is still completely surrounded by the air; however, the thin film of air persists for less than a millisecond before it breaks down at discrete locations and is followed by the formation of multiple liquid bridges that then spread rapidly and completely wet the surface beneath the drop[19]. The formation of the dimple has been well characterized both theoretically[26] and experimentally[48, 49, 5]; however, much less is known about the dynamics of the thin film of air and the mechanism for its breakdown. As the breakdown of the thin film of air may depend significantly on the chemical and geometrical properties of the surface, it is of value to investigate the stability of the thin film of air on surfaces for which these properties are known.

In this Letter we show that upon impacting a freshly cleaved mica surface, the thin film of air separating the liquid from the surface persists for up to tens of milliseconds. Moreover, if the impact velocity is below a critical value V_c then the drop will completely rebound off of the perfectly hydrophilic mica surface. The thickness of the thin film of air decreases with time, yet the film remains remarkably stable and breaks down only when the liquid is within a few nanometers of the surface. Thus, if the drainage of the thin film of air occurs more slowly than half of the oscillation time of the liquid drop $\tau = 2.2 * (\rho R^3 / \gamma)^{1/2}$ [34], then the drop will lift off before the

thin film of air breaks down, and will bounce away from the surface.

In order to understand the role played by air during the earliest stages of the droplet impact event, we use a variant of Total Internal Reflection (TIR) microscopy and directly observe the impact surface, as shown schematically in Fig. 4.1a. We illuminate the surface of a dove prism¹ from below with a monochromatic, collimated light source at an angle of incidence greater than the critical angle for total internal reflection, thus exciting an evanescent wave above the surface of the prism with a characteristic decay length, $\delta \sim \mathcal{O}(100 \text{ nm})$. We use a long working distance objective to image the beam as it exits the prism on to our fast camera's imaging sensor. When the droplet enters the evanescent field, light partially transmits to the drop, resulting in a grayscale on the recorded image, as shown in a typical TIR image of an impacting droplet in Fig. 4.1c. The image intensity, $I(x, y, t)$ is normalized and converted to height as $z = -\delta \log \left(1 - \frac{I(x, y, t)}{I(x, y, 0)} \right)$ [19]; a typical example of a surface profile is shown in Fig. 4.1d.

As explained above, impacting drops do not make immediate contact with the substrate; instead, a thin film of air forms beneath the drop, supporting the liquid as it spreads over the surface. As the drop approaches the substrate a dimple of compressed air is formed at the bottom of the drop. TIR offers superb resolution at nanometer scales, but its range is limited and therefore our technique cannot resolve the dynamics occurring more than 500nm above the surface; thus, the development of the dimple cannot be resolved using TIR. As a result, the liquid enters the evanescent field after the dimple has already formed, and appears as a sharp ring, as shown in the

¹The surface of the prism is optically coupled to the impact surface using microscope objective immersion oil (Zeiss 518 f).

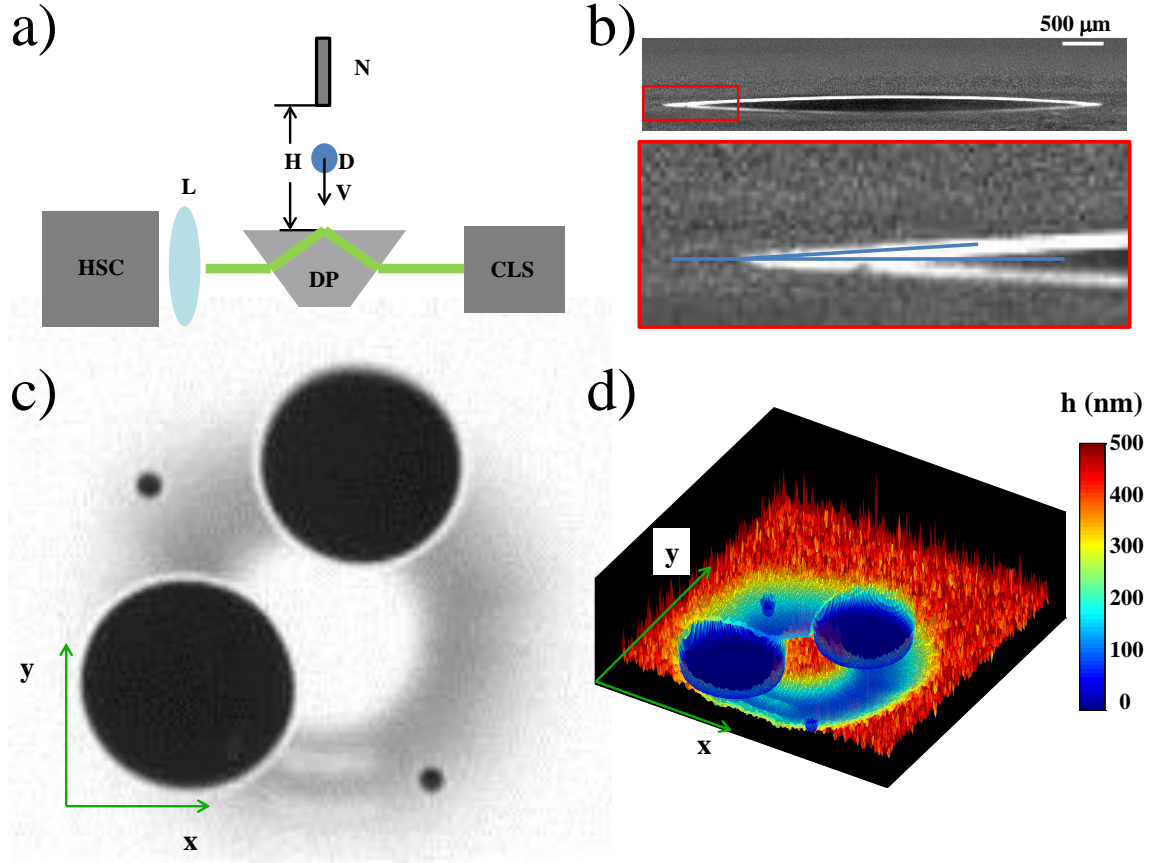


Figure 4.1: : The experimental system. (a) A schematic of the experimental setup. Drops (D) of 10 cSt water-glycerol solution, with a radius of $800 \mu\text{m}$ fall from a nozzle (N), from a height (H) above the substrate, whereupon the drop impacts with a velocity ($V = (2gH)^{1/2}$). Monochromatic light emitted from a collimated light source (CLS) enters a dove prism (DP) from the side and totally internally reflects from the glass-air interface immediately beneath the impacting drop, and then exits the prism. The interface is imaged through a long-working distance microscope objective (L), and recorded with a Phantom v711 fast camera (HSC) at frame rates exceeding 150 kHz. (b) The liquid drop totally wets the freshly cleaved, hydrophilic mica surface. (c) A typical snapshot from a drop impact event, the gray ring indicates the presence of a nanometer thin film of air above the surface and the four black circles are locations where the solid liquid contact occurred. (d) same as (c) only the gray scale is converted to height and presented as a surface plot with color indicating height in nanometer above the mica surface

fast-camera snapshot in Fig. 4.2a i. As more fluid funnels outward, it rapidly skates over the thin film of air, increasing the film's lateral dimension, as shown in Fig.4.2a ii; strikingly, the inner radius of the thin film of air remains nearly constant. Ultimately, the liquid front arrests and the drop stops expanding as it reaches its greatest lateral extent, r^* , as shown in Fig.4.2a iii. The dark gray ring at the perimeter of the thin film of air is indicative that at the final stage of spreading the liquid gets nearer to the surface. These dynamics are universal and are typical to all bouncing drops.

4.1 The kinematics of the liquid-air interface

The entire dynamics of the liquid skating over a thin film of air can be represented in a single kymograph, as shown for a typical experiment in Fig. 4.2b. We exploit the radial symmetry of the spreading dynamics to calculate an instantaneous height-radius profile, $h(r)$ and take an azimuthal average over a wedge, as indicated by the red segment in Fig. 4.2ai. We then plot these profiles in series to obtain the kymograph, wherein height is encoded in color from dark blue to bright red. The inner boundary of the thin film of air, r_e , remains remarkably stationary throughout the spreading dynamics. This is in striking contrast to the closure of the dimple driven by wetting, in the cases reported for impact on glass surfaces, where contact initiated. The liquid spreads outward away from the impact center as the thin film of air grows, indicated by the expanding blue region in the figure; the outer boundary of the spreading liquid grows initially as $t^{1/2}$. The liquid decelerates and eventually halts after a time t^* 1.8 msec from initiation of impact, and at a radial distance r^* $900\mu\text{m}$, as indicated in Fig. 4.2b by the horizontal and vertical white dashed lines, respectively.

Importantly, after the liquid skates over the surface, forming the thin film of air, it continues to slowly approach the surface as the air drains, as shown in Fig. 4.2b by the deepening shades of blue. The impact of the drop onto the surface deforms the drop appreciably, and it wobbles and oscillates. t^* decreases with increasing impact velocity V , as shown in Fig.4.2c. Nevertheless, although t^* decreases, the thin film of air spreads wider as the velocity of impact increases, as shown by the increasing difference between r^* and r_e in Fig. 4.2d. The minimal thickness of the thin film of air, h_m , varies strongly for $V < 0.6$ m/sec; however, for $V > 0.6$ m/sec, h_m remains nearly constant, as shown in Fig. 4.2e.

4.2 Characteristic timescale for rebound

As the impact dynamics unfold, the thin film of air remains stable in spite of its diminutive thickness. To probe the dynamics of rebound, we compare images of identical rebounding drops from two experiments: one imaged from the side and the other with TIR, as shown in Fig. 4.3 a. At $t^* = 1.8$ msec, the droplet has spread to r^* , and a dark gray ring appears at the rim of the thin film of air; by this time the drop has deformed significantly from its originally spherical shape into an oblatum, as shown in Fig. 4.3a ii. After spreading to r^* , the drop begins to retract from the surface; 3.6 msec after its initial approach to within nanometers of the surface, the drop is ascending, as the radius of the film of air decreases to less than half of its greatest lateral extent, as shown in Fig. 4.3a iii. Ultimately, after 5.7 msec have elapsed, the droplet completely exits the evanescent field, rebounding from the surface, as shown in Fig. 4.3a.iv. The liquid front spreads outward as $t^{1/2}$ [40], but retracts at a

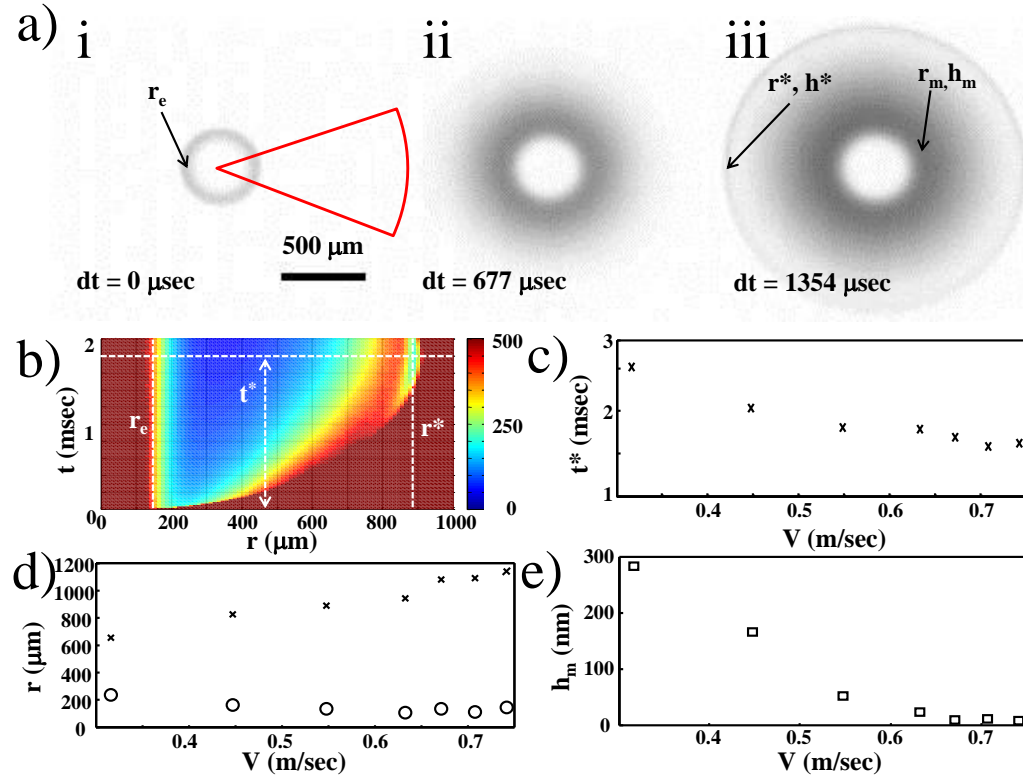


Figure 4.2: : Impact dynamics of the drop. (a) Three consecutive TIR images corresponding to a drop impacting on a mica substrate with $H = 15\text{mm}$ ($V = 0.55 \text{ m/sec}$). The red wedge is an annular region over which the height profiles are averaged, converted from grayscale to height and then shown as an $r-t$ plot in (b). Here, $dt=0$ corresponds to the first frame where the liquid has entered within 500 nm of the surface. (b) An $r-t$ plot for the entire impact event shown in (a), where color represents height from 0 to 500 nm . t^* indicates the total liquid spreading time; r^* and r_e are the greatest radial extent of the spreading liquid and the radial edge of the dimple, respectively. (c) t^* as a function V . (d) r^* and r_e are shown as a function of V . (e) The height of the film at closest approach h_m , indicated in (a) iii., as a function of V .

nearly constant rate, $V_{rec} \sim 0.2\text{m/s}$, indicated by the line in Fig. 4.3b. As a result of this asymmetry in the spreading rates, the outward spreading of the liquid lasts ~ 1.8 msec, while its retraction persists for approximately double the spreading time, as shown in the figure. $V_{rec} \sim 0.2\text{m/s}$ remains practically unchanged for all impact velocities, as shown in the inset to Fig.4.3b.

In spite of the asymmetry between the spreading and the retracting of the drop, the overall time it takes the drop to complete a bouncing cycle, t_l , depends on R but not on V and is in remarkably good agreement with the value for the period of an oscillating drop, $\tau = 2.22(\rho * r^3 / \gamma)^{1/2}$ calculated by Lord Rayleigh and shown in Fig. 4.3c. This agreement with the calculated pre-factor for drops rebounding from the thin film of air is also surprisingly inconsistent with the 20% difference reported for rebound from superhydrophobic surfaces[39]. Due to viscous losses, during rebound not all the energy is conserved, so the bouncing drop does not recover its original impact speed. We estimate the coefficient of restitution, C_R by measuring the original release height, H_f , and the maximal rebounding height, H_r and calculating $\sqrt{H_r/H_f}$; this ratio is a good proxy for the more commonly used definition of C_R , V_r/V . C_R is independent of R , but decreases with V , as shown in Fig. 4.3d. In our experiments C_R never exceeds 0.65; this is almost 30% lower than the value of $C_R = 0.9$, indicated by the dashed line of Fig. 4.3d, which is measured for impact on superhydrophobic surfaces.

4.3 Enhanced dissipation in the thin film of air

To understand the much lower C_R relative to that seen in bouncing from a superhydrophobic surface, we note that the motion of the fluid drop induces large shear rates in the thin air layer that separates the fluid and solid. This is potentially a source of dissipation that can take away energy from the drop. In addition, there is another source of dissipation in system, due to shear in the drop itself. We estimate the viscous power per unit length associated the retracting liquid front of radius r_e as $\mu_{liq} \left(\frac{U}{r_e}\right)^2 r_e^2$ and the viscous power associated with the shear in the air layer as $\mu_{air} \left(\frac{U}{h}\right)^2 h r_e$. These become comparable when the air film thickness is of order $h^* = \frac{\mu_{gas}}{\mu_{liq}} r_e$; in our experiment, with 10cSt water-glycerol withdrawing from air and $r_e \sim \mathcal{O}(100\mu\text{m})$, we expect dissipation to be dominant in the air for $h^* \lesssim \mathcal{O}(200\text{ nm})$. This cross-over height is between the film thicknesses we observe above the mica surfaces, and the height of the pillars used to make superhydrophobic surfaces that exhibit reduced drag. Counter-intuitively, drops rebound from sparse contacts with superhydrophobic surfaces more vigorously than from mica surfaces, where there is absolutely no contact, but a thinner layer of air.

During the retraction phase, as the drop begins to lift off of the surface, and air must enter the thin gap between the solid and liquid. Balancing the viscous power per unit length with the driving power due to capillary forcing at the retracting front yields $\mu_{air} \left(\frac{U}{h}\right)^2 h \ell \sim \frac{\gamma}{r_e} U \ell$; thus, $U = \frac{h\gamma}{\mu_{air} r_e} \sim \frac{10\text{ nm } 0.07\text{ J/m}^2}{2 \times 10^{-5}\text{ Pa s } 100\mu\text{m}} \sim 0.35\text{ m/sec}$. For typical values of the experimental parameters, the retraction velocity is in qualitative agreement with the measured value of $U \sim 0.25\text{ m/sec}$, independent of the radial distance of the retracting front from the impact center, in agreement with our mea-

surements plotted in the inset of Fig. 4.3 (c).

The thin film of air formed beneath a liquid drop impacting on an atomically smooth mica surface exhibits remarkable stability. If the liquid is suspended by the air at a sufficiently large distance from the surface such that interfacial forces are small, the thin film of air will persist throughout the entire oscillation of the drop, and the drop will bounce away from the surface. However, if the film of air is thin enough then surface forces acting between the solid and the liquid induce an instability in the thin film of air, and it breaks down by the formation of multiple liquid bridges that bind the drop to the surface, as shown in Fig. 4.4a, preventing it from bouncing. At high enough impact velocities, the initial thickness of the air film is significantly reduces and thus the film may drain to a critical thickness, h_c , within nanometers of the surface and subsequently rupture², as shown in Fig. 4.4b for a thin film with an initial thickness of 10nm. h_c does not depend on impact velocity, as shown in Fig. 4.4c. The single value of h_c indicates that the mechanism for the breakdown of the thin film of air is likely to be dominated by surface forces. Our minute, few nanometer values of h_c measured above mica surfaces are significantly lower than the scales measured for impact on glass surfaces, which can exceed 400 nm[12]; we attribute this discrepancy to geometric defects on the glass surface that nucleate points of contact. Note that for hydrophilic surfaces, any single asperity will nucleate a liquid bridge that will rapidly spread and destroy the entire thin film of air; thus, although commercial glass surfaces can in fact be very smooth on average, for the thin film of air to persist the glass must be absolutely smooth over a macroscopically large

²The stability of the thin film of air is discussed in greater detail in App. C

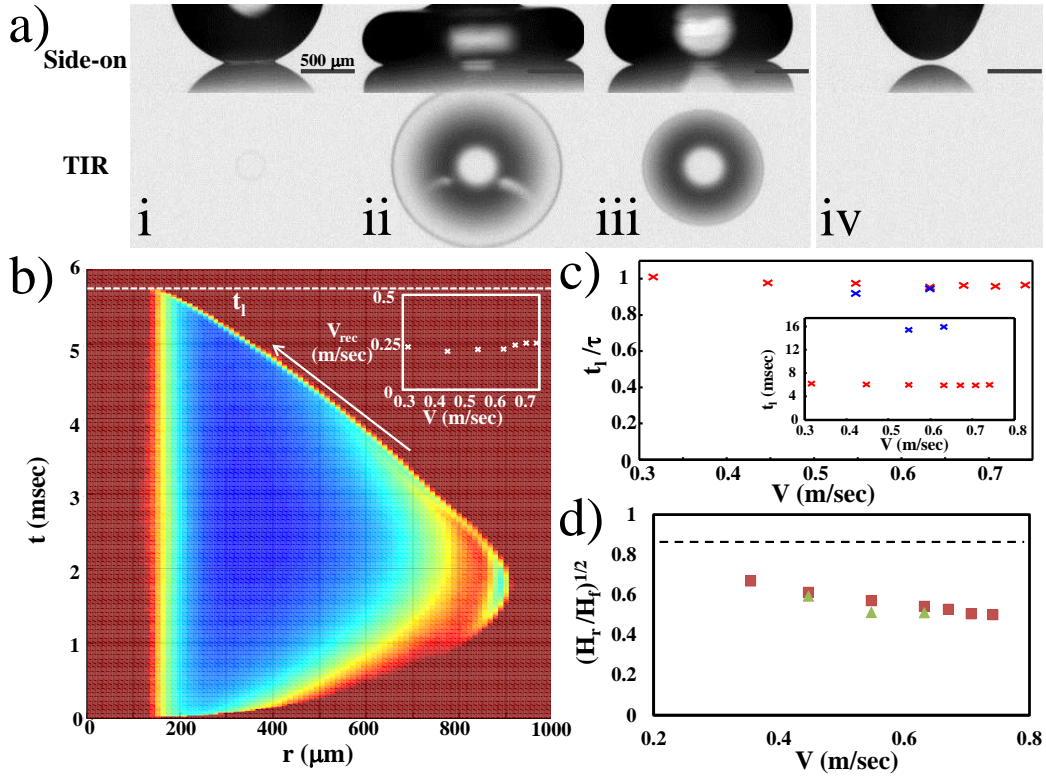


Figure 4.3: : Drops bouncing off of mica surfaces. (a) A montage of fast camera images taken from the side (top) and with TIR (bottom) of two identical experiments with $R = 800\mu\text{m}$ and $H = 15\text{mm}$. Frames i-iii are taken at an interval of 1.8 msec; frame iv is taken 6.5 msec after the first frame. (b) A $r - t$ plot of the experiment shown in (a), color scale is as in Fig. 4.2b. The liquid entirely departs the evanescent field at $t = t_l$. The liquid retracts inwards at velocity V_{rec} , indicated by the white arrow; (inset) V_{rec} as a function of V . (c) The drop residency time scaled by the drop oscillation period, t_l/τ as a function of V for two drop radii: $R = 0.8$ mm (red 'x') and $R = 1.6$ mm (blue 'x') (inset) t_l as a function of V . (d) The coefficient of restitution C_R as a function of V .

area. While this is readily achieved with freshly cleaved mica, it does not consistently occur for glass. However, if the surface is indeed absolutely smooth, we can now establish a criterion for the transition from bouncing to immediate contact: if the thin film of air can drain to a thickness below h_c before $t = \tau$ then contact will occur, binding the drop to the surface and thus preventing rebound. This is demonstrated by the black curves in Fig. 4.4d. However, if the thin film of air does not reach the critical thickness before $t = \tau$, then the liquid drop will completely rebound, as demonstrated by the red curves in in Fig. 4.4d.

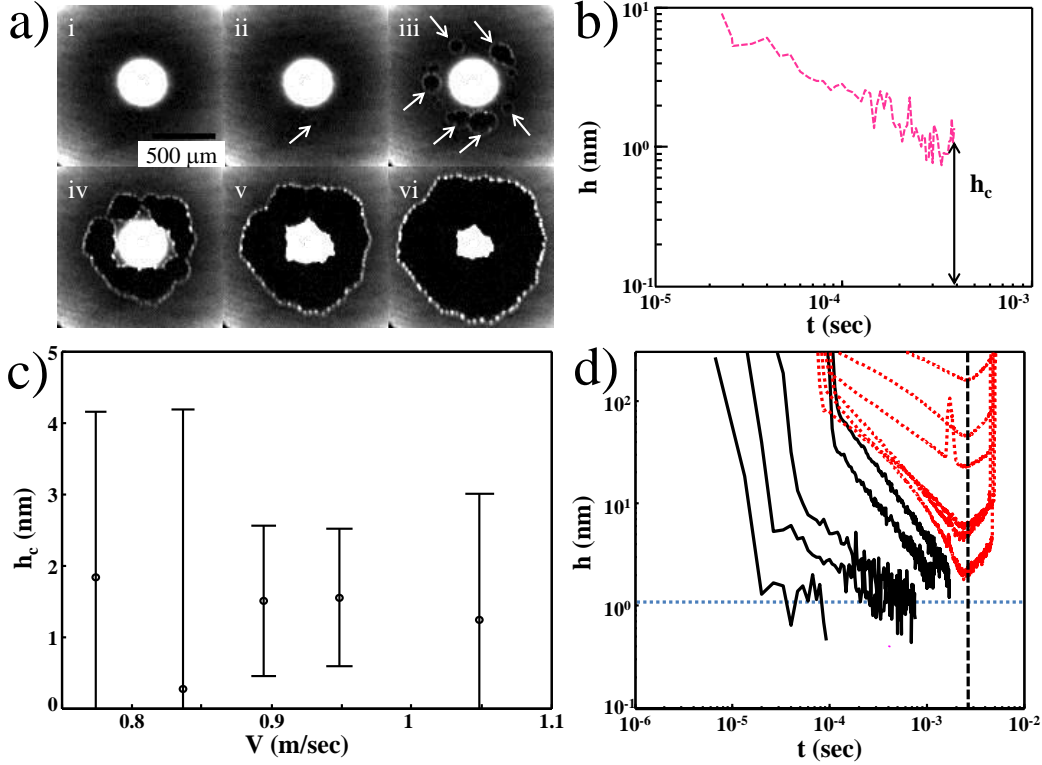


Figure 4.4: : Stability and breakdown of the thin film of air. (a) A sequence of typical images for a $R = 800\mu\text{m}$ drop impacting at $V = 0.89\text{ m/sec}$. In order to highlight the dynamics occurring less than 10nm above the surface, contrast is enhanced and white corresponds to all heights greater than 17.5nm . Contact is depicted by bright rings and initiates at discrete points in ii; the contacts subsequently grow in iii, and merge into a closed ring in iv. The contacts continue to grow outward and inward from the ring in v-vi. Subsequent images are separated by $27\mu\text{sec}$. (b) $h(t)$ at a point where contact initiated for $R = 800\mu\text{m}$ and $V = 0.94\text{ m/sec}$. The initial film thickness is 5.5nm and the film ruptures at $h_c = 1\text{nm}$. (c) Rupture height, h_c , as a function of V for $R = 800\mu\text{m}$. for $V < V_c = 0.75$ the film never ruptures and the drops bounce away from the surface. (d) $h(t)$ traces below (red) above (black) the critical velocity for droplet bouncing $V_c = 0.75\text{ m/sec}$. The typical reversal time, t^* , and h_c are indicated the vertical dashed line horizontal dotted line respectively.

Bibliography

- [1] Daniel Attinger, Craig Moore, Adam Donaldson, Arian Jafari, and Howard A Stone. Fluid dynamics topics in bloodstain pattern analysis: Comparative review and research opportunities. *Forensic science international*, 231(1):375–396, 2013.
- [2] Gloria A Bach, Donald L Koch, and Arvind Gopinath. Coalescence and bouncing of small aerosol droplets. *Journal of fluid mechanics*, 518(1):157–185, 2004.
- [3] Anne-Laure Bianco, Christophe Clanet, and David Quéré. First steps in the spreading of a liquid droplet. *Physical Review E*, 69(1):016301, 2004.
- [4] James C Bird, Shreyas Mandre, and Howard A Stone. Short-time dynamics of partial wetting. *Physical review letters*, 100(23):234501, 2008.
- [5] Wilco Bouwhuis, Roeland CA van der Veen, Tuan Tran, Diederik L Keij, Koen G Winkels, Ivo R Peters, Devaraj van der Meer, Chao Sun, Jacco H Snoeijer, and Detlef Lohse. Maximal air bubble entrainment at liquid-drop impact. *Phys. Rev. Lett.*, 109(26):264501, 2012.
- [6] M Bussmann, J Mostaghimi, and S Chandra. On a three-dimensional volume tracking model of droplet impact. *Physics of Fluids*, 11:1406, 1999.
- [7] S Chandra and CT Avedisian. On the collision of a droplet with a solid surface. *Proceedings: Mathematical and Physical Sciences*, pages 13–41, 1991.
- [8] GE Cossali, A Coghe, and M Marengo. The impact of a single drop on a wetted solid surface. *Experiments in fluids*, 22(6):463–472, 1997.
- [9] Y Couder, E Fort, C-H Gautier, and A Boudaoud. From bouncing to floating: Noncoalescence of drops on a fluid bath. *Physical review letters*, 94(17):177801, 2005.
- [10] Laurent Courbin, James C Bird, Mathilde Reyssat, and Howard A Stone. Dynamics of wetting: from inertial spreading to viscous imbibition. *J. Phys. Condens. Matter*, 21(46):464127, 2009.

- [11] Pierre-Gilles De Gennes, Françoise Brochard-Wyart, and David Quéré. *Capillarity and wetting phenomena: drops, bubbles, pearls, waves*. Springer, 2004.
- [12] Jolet de Ruiter, Jung Min Oh, Dirk van den Ende, and Frieder Mugele. Dynamics of collapse of air films in drop impact. *Physical review letters*, 108(7):074505, 2012.
- [13] Michelle M Driscoll and Sidney R Nagel. Ultrafast interference imaging of air in splashing dynamics. *Physical Review Letters*, 107(15):154502, 2011.
- [14] Michelle M Driscoll, Cacey S Stevens, and Sidney R Nagel. Thin film formation during splashing of viscous liquids. *Physical Review E*, 82(3):036302, 2010.
- [15] Seogheon Ham, Wunki Jung, Seunghyun Lim, Yonghee Lee, and Gunhee Han. A complementary metal-oxide-semiconductor image sensor with analog gamma correction using a nonlinear single-slope analog-to-digital converter. *Jpn. J. Appl. Phys.*, 45:2522, 2006.
- [16] Y Hardalupas, AMKP Taylor, and JH Wilkins. Experimental investigation of sub-millimetre droplet impingement on to spherical surfaces. *International journal of heat and fluid flow*, 20(5):477–485, 1999.
- [17] JN Israelachvili. *Intermolecular and Surface Forces*. Academic Press, New York, 1985.
- [18] C Josserand, L Lemoyne, R Troeger, and S Zaleski. Droplet impact on a dry surface: triggering the splash with a small obstacle. *Journal of fluid mechanics*, 524:47–56, 2005.
- [19] John M Kolinski, Shmuel M Rubinstein, Shreyas Mandre, Michael P Brenner, David A Weitz, and L Mahadevan. Skating on a film of air: drops impacting on a surface. *Physical Review Letters*, 108(7):074503, 2012.
- [20] Aurélie Lafuma and David Quéré. Superhydrophobic states. *Nature materials*, 2(7):457–460, 2003.
- [21] Andrzej Latka, Ariana Strandburg-Peshkin, Michelle M Driscoll, Cacey S Stevens, and Sidney R Nagel. Creation of prompt and thin-sheet splashing by varying surface roughness or increasing air pressure. *Physical Review Letters*, 109(5):054501, 2012.
- [22] Min Lee, James CY Dunn, and Benjamin M Wu. Scaffold fabrication by indirect three-dimensional printing. *Biomaterials*, 26(20):4281–4289, 2005.
- [23] MB Lesser. Analytic solutions of liquid-drop impact problems. *Proc. R. Soc. A*, 377(1770):289–308, 1981.

- [24] MB Lesser and JE Field. The impact of compressible liquids. *Annual review of fluid mechanics*, 15(1):97–122, 1983.
- [25] Shreyas Mandre and Michael P Brenner. The mechanism of a splash on a dry solid surface. *Journal of Fluid Mechanics*, 690:148–172, 2012.
- [26] Shreyas Mandre, Madhav Mani, and Michael P Brenner. Precursors to splashing of liquid droplets on a solid surface. *Physical review letters*, 102(13):134502, 2009.
- [27] Madhav Mani, Shreyas Mandre, and Michael P Brenner. Events before droplet splashing on a solid surface. *J. Fluid Mech.*, 647(163):112, 2010.
- [28] V Mehdi-Nejad, J Mostaghimi, and S Chandra. Air bubble entrapment under an impacting droplet. *Physics of fluids*, 15:173, 2003.
- [29] A.L.N. Moreira and A.S. Moita. *Handbook of Atomization and Sprays*, chapter Droplet-Wall Interactions. Springer Science+Business Media, 2011.
- [30] CHR Mundo, M Sommerfeld, and C Tropea. Droplet-wall collisions: experimental studies of the deformation and breakup process. *International journal of multiphase flow*, 21(2):151–173, 1995.
- [31] T Onda, S Shibuichi, N Satoh, and K Tsujii. Super-water-repellent fractal surfaces. *Langmuir*, 12(9):2125–2127, 1996.
- [32] CO Pedersen. An experimental study of the dynamic behavior and heat transfer characteristics of water droplets impinging upon a heated surface. *International Journal of Heat and Mass Transfer*, 13(2):369–381, 1970.
- [33] Kai Range and François Feuillebois. Influence of surface roughness on liquid drop impact. *Journal of colloid and interface science*, 203(1):16–30, 1998.
- [34] Lord Rayleigh. On the capillary phenomena of jets. *Proc. R. Soc.*, 29(196-199):71–97, 1879.
- [35] Martin Rein. Phenomena of liquid drop impact on solid and liquid surfaces. *Fluid Dynamics Research*, 12(2):61–93, 1993.
- [36] Martin Rein and Jean-Pierre Delplanque. The role of air entrainment on the outcome of drop impact on a solid surface. *Acta mechanica*, 201(1-4):105–118, 2008.
- [37] Günter Reiter. Dewetting of thin polymer films. *Phys. Rev. Lett.*, 68(1):75, 1992.
- [38] D Richard and D Quéré. Bouncing water drops. *Europhys. Lett.*, 50(6):769, 2000.

- [39] Denis Richard, Christophe Clanet, and David Quéré. Surface phenomena: Contact time of a bouncing drop. *Nature*, 417(6891):811–811, 2002.
- [40] Romain Rioboo, Cameron Tropea, and Marco Marengo. Outcomes from a drop impact on solid surfaces. *Atomization and Sprays*, 11(2), 2001.
- [41] Ilia V Roisman, Romain Rioboo, and Cameron Tropea. Normal impact of a liquid drop on a dry surface: model for spreading and receding. *Proceedings of the Royal Society of London. Series A: Mathematical, Physical and Engineering Sciences*, 458(2022):1411–1430, 2002.
- [42] Shmuel M Rubinstein, Gil Cohen, and Jay Fineberg. Detachment fronts and the onset of dynamic friction. *Nature*, 430(7003):1005–1009, 2004.
- [43] Ji San Lee, Byung Mook Weon, Jung Ho Je, and Kamel Fezzaa. How does an air film evolve into a bubble during drop impact? *Physical review letters*, 109(20):204501, 2012.
- [44] Paul Schmidt and Günter Knauss. Prallzerstäubung von flüssigkeiten bei nicht-benetzung. *Chemie Ingenieur Technik*, 48(7):659–659, 1976.
- [45] Robert D Schroll, Christophe Josserand, Stéphane Zaleski, and Wendy W Zhang. Impact of a viscous liquid drop. *Phys. Rev. Lett.*, 104(3):034504, 2010.
- [46] Satoshi Shibuichi, Tomohiro Onda, Naoki Satoh, and Kaoru Tsujii. Super water-repellent surfaces resulting from fractal structure. *The Journal of Physical Chemistry*, 100(50):19512–19517, 1996.
- [47] CD Stow and MG Hadfield. An experimental investigation of fluid flow resulting from the impact of a water drop with an unyielding dry surface. *Proceedings of the Royal Society of London. A. Mathematical and Physical Sciences*, 373(1755):419–441, 1981.
- [48] ST Thoroddsen, TG Etoh, and K Takehara. Air entrapment under an impacting drop. *Journal of Fluid Mechanics*, 478:125–134, 2003.
- [49] ST Thoroddsen, TG Etoh, K Takehara, N Ootsuka, and Y Hatsuki. The air bubble entrapped under a drop impacting on a solid surface. *J. Fluid Mech.*, 545:203–212, 2005.
- [50] ST Thoroddsen and Jun Sakakibara. Evolution of the fingering pattern of an impacting drop. *Physics of fluids*, 10:1359, 1998.
- [51] ST Thoroddsen, K Takehara, and TG Etoh. Bubble entrapment through topological change. *Phys. Fluids*, 22(5):051701–051701, 2010.

- [52] Peichun Tsai, Roeland CA van der Veen, Matthias van de Raa, and Detlef Lohse. How micropatterns and air pressure affect splashing on surfaces. *Langmuir*, 26(20):16090–16095, 2010.
- [53] Dirkjan B van Dam and Christophe Le Clerc. Experimental study of the impact of an ink-jet printed droplet on a solid substrate. *Physics of Fluids*, 16:3403, 2004.
- [54] Roeland CA van der Veen, Tuan Tran, Detlef Lohse, and Chao Sun. Direct measurements of air layer profiles under impacting droplets using high-speed color interferometry. *Physical Review E*, 85(2):026315, 2012.
- [55] Roeland CA van der Veen, Tuan Tran, Detlef Lohse, and Chao Sun. Direct measurements of air layer profiles under impacting droplets using high-speed color interferometry. *Physical Review E*, 85(2):026315, 2012.
- [56] Randy L Vander Wal, Gordon M Berger, and Steven D Mozes. Droplets splashing upon films of the same fluid of various depths. *Experiments in fluids*, 40(1):33–52, 2006.
- [57] Randy L Vander Wal, Gordon M Berger, and Steven D Mozes. The splash/non-splash boundary upon a dry surface and thin fluid film. *Experiments in fluids*, 40(1):53–59, 2006.
- [58] F. Vrij, A. Hesselink and H. Van Der Tempel. *Koninkl Nederl. Academie van Wetenschappen Amsterdam B*, 73, 1970.
- [59] Peter Walzel. Zerteilgrenze beim tropfenprall. *Chemie Ingenieur Technik*, 52(4):338–339, 1980.
- [60] AM Worthington. On the forms assumed by drops of liquids falling vertically on a horizontal plate. *Proceedings of the royal society of London*, 25(171-178):261–272, 1876.
- [61] Arthur Mason Worthington. *The splash of a drop*. Society for Promoting Christian Knowledge London, 1895.
- [62] F Brochard Wyart and J Daillant. Drying of solids wetted by thin liquid films. *Canadian Journal of Physics*, 68(9):1084–1088, 1990.
- [63] Lei Xu. Liquid drop splashing on smooth, rough, and textured surfaces. *Physical Review E*, 75(5):056316, 2007.
- [64] Lei Xu, Loreto Barcos, and Sidney R Nagel. Splashing of liquids: Interplay of surface roughness with surrounding gas. *Physical Review E*, 76(6):066311, 2007.

- [65] Lei Xu, Wendy W Zhang, and Sidney R Nagel. Drop splashing on a dry smooth surface. *Physical review letters*, 94(18):184505, 2005.
- [66] AL Yarin. Drop impact dynamics: splashing, spreading, receding, bouncing. *Annu. Rev. Fluid Mech.*, 38:159–192, 2006.

Appendix A

Experimental methods and details of the calculated velocity for liquid spreading

A.1 TIR Measurement

To observe the thin film of air, the top surface of a dove prism (BK7 glass) is illuminated with a collimated light source (Thor labs LED model M530L2 or a red HeNe laser, 10 mW), at an angle of incidence greater than the angle for total internal reflection (TIR) of the glass-air interface and lesser than the angle of total internal reflection of the glass-liquid (IPA) interface; thus, an exponentially decaying evanescent field forms above the reflecting surface. The characteristic decay length of the evanescent field depends on the wavelength of the light, the indices of refraction of the glass and air, and the incidence angle. The incidence angle is typically 45 degrees,

corresponding to a characteristic decay length $\delta \sim 100$ nm. The light is recorded on the camera's imaging sensor after it reflects off of the surface of the prism, resulting in a point-wise intensity measurement, $I(x, y, t)$. As the droplet enters the evanescent field, less light is reflected, and the liquid appears as a gray scale on the camera's imaging sensor. This directly probes the thin layer of air. There is a region in the image that routinely captures a multiply reflected beam, directly above the impact center as viewed in the images recorded by the camera's imaging sensor. The reflected beams appears in the VFT images of Fig. 2.3 as a rectangular gray region. In this region only, the mapping from intensity to height for individual frames is not valid. The reflected light is recorded using a Phantom v 7.3 high speed camera, which has a CMOS sensor with 14-bit depth; images are captured at rates up to 150000 frames per second, with a minimal exposure time of $1 \mu\text{s}$. The recorded intensity is mapped to height using the following relationship: $h(x, y, t) = -\delta \log \left(1 - \frac{I(x, y, t)}{I(x, y, 0)} \right)$, where $I(x, y, 0)$ is the intensity before the droplet enters the evanescent field; normalizing $I(x, y, t)$ by $I(x, y, 0)$ subtracts the background and improves the signal to noise ratio.

A.2 The Virtual Frame Technique

In many cases, even everyday phenomena occur over time scales too rapid to be captured by even the fastest high speed camera. Examples of this are numerous and include: the impact, breakup and coalescence of fluid droplets, dynamic fractures and electrical discharge of gasses. To overcome the inherent limitations of the frame rate of the fastest high speed cameras, we introduce a completely new imaging method, which we call the Virtual Frame Technique (VFT). VFT enables real time visualization of

many such systems using a standard camera. Moreover, unlike conventional fast cameras that require a compromise between spatial resolution and speed, with VFT, the full spatial resolution of the camera is preserved.

To use VFT, the visualization setup must first be adapted to produce an approximately binary signal. This can be achieved in many different ways; in our study of droplet impact, TIR results in nearly binary contrast between wetted and un-wetted surface, changing from completely bright to completely dark as soon as liquid-solid contact occurs. Also, a propagating crack front can be translated into a binary signal by imaging the silhouette of an opaque material against a brightly lit background. VFT exploits this binary contrast by increasing the camera exposure time to integrate over times longer than the characteristic dynamics under the strict assumption that the dynamics remain irreversible within the integration time, thus ensuring that the intensity at any given position directly reflects the total time until the signal was switched from 0 to 1 (or 1 to 0). Thus, all pixels of equal grayscale value are in fact isochrones, and consecutive binary contrast thresholds provide what is essentially a series of virtual frames capturing the entire dynamics. The assumption that once intensity at a pixel is switched from 0 to 1 (or 1 to 0) it will remain that constant for the remainder of the integration time is essential and guarantees that intensity can be uniquely mapped to time. The temporal resolution of the acquisition is set by the dynamic range of the camera and for some imaging sensors[15] can be further improved by exploiting the gamma correction, which alters the exponent of the sensor response function; for a decelerating dynamics, gamma can be set to a value smaller than one, so that the temporal resolution is initially highest. Ideal applications of

VFT include phenomena requiring temporal resolution in the 1-100 MHz range, for which the salient dynamics are irreversibly progressing fronts.

A.3 Photodiode measurement

For high-velocity drop impacts (velocities greater than 1 m/s), the dynamics of the air film dewetting the surface occur too rapidly to be regularly observed with the Phantom v 7.3 fast camera; serendipitously, however, the air film formation occasionally occurs during the microsecond exposure of the camera, confirming its existence. In order to measure the dynamics of the air layer, the full-frame imaging of the camera is supplemented with an ultra-fast, single-point intensity measurement, recorded with a photodiode¹. The photodiode and camera are in conjunction with a cube beam splitter: half of the intensity is recorded on the camera's imaging sensor, while a portion of the remaining half of the intensity is sampled by the photodiode, as shown in the schematic in Fig. A.1.

The position and size of the area sampled by the photodiode relative to the camera's imaging sensor is precisely identified to within ~ 4 microns by scanning a point probe over the interface. Two such photodiode locations are illustrated by colored circles in Fig. A.2(a); the images shown correspond to the impact of a drop released from $H = 21$ cm. The second frame clearly shows that even at these high impact velocities, a transient film is formed prior to contact. The actual area sampled by the photodiode depends on the magnification of the objectives we use (5x to 20x) as well

¹The single-point intensity is recorded with an amplified Thorlabs photodiode, model PDA10A; the signal generated by the photodiode is recorded with a Tektronics 100 MHz oscilloscope, model no. TDS3014C

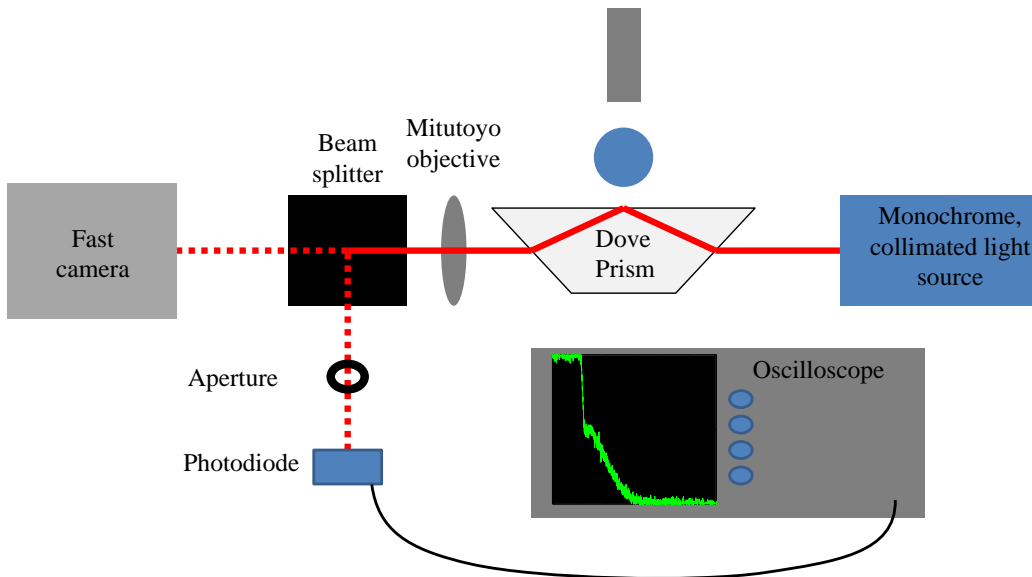


Figure A.1: A schematic of the experimental set-up for the photodiode measurement. A beam splitter divides the intensity of the reflected light after it exits the prism, such that half of the light is imaged on the camera's sensor, and a portion of the remaining half of the intensity is sampled by the photodiode at up to 100 MHz. The remaining portion sampled by the photodiode can be restricted with an aperture. The intensity trace is recorded with an oscilloscope, which is set to trigger at a threshold intensity.

as the opening of an adjustable aperture behind the objective. The diameter of the sampled area for the 10x objective used for all experiments shown, is $60 \mu\text{m}$. In our setup, there is an unavoidable variability in the location of the impact center, which for drops falling from $H = 21 \text{ cm}$ is approximately $500 \mu\text{m}$; however, the variability in the impact location provides a convenient means of probing the dynamics of the spatially extended air layer with the added temporal resolution of the photodiode without the need to displace the diode. We dropped hundreds of drops from $H = 21 \text{ cm}$, and recorded the intensity traces as well as individual frames from the camera; of these data, there were several experiments that were ideally positioned to accurately measure the first moments of impact beneath and around the rim of the central air pocket with the photodiode; additionally, an occasional snapshot of the air layer was also captured in the image sequence, as shown in the second frame of Fig. A.2(a)

We identify two distinct types of intensity traces and plot them in Fig. A.2(b); The first type of intensity trace, plotted in green and labeled 1i and 1ii, is acquired in cases where the photodiode is measuring the intensity over a region that is partially beneath the thin film of air and partially beneath the dimple, where the liquid is too high above the surface and does not affect the intensity of the light reflected from underneath the dimple, as can be seen by the bright, white spots in the center of impact as recorded in the camera images. The second type of trace, plotted in red and labeled 2i and 2ii, corresponds to a measurement by the photodiode of an area completely outside of the dimple; thus, providing a measurement of the dynamics beneath the outward-moving liquid. For the first type of trace, we observe three distinctive regions: I, a rapid intensity drop followed by II, a plateau similar to the

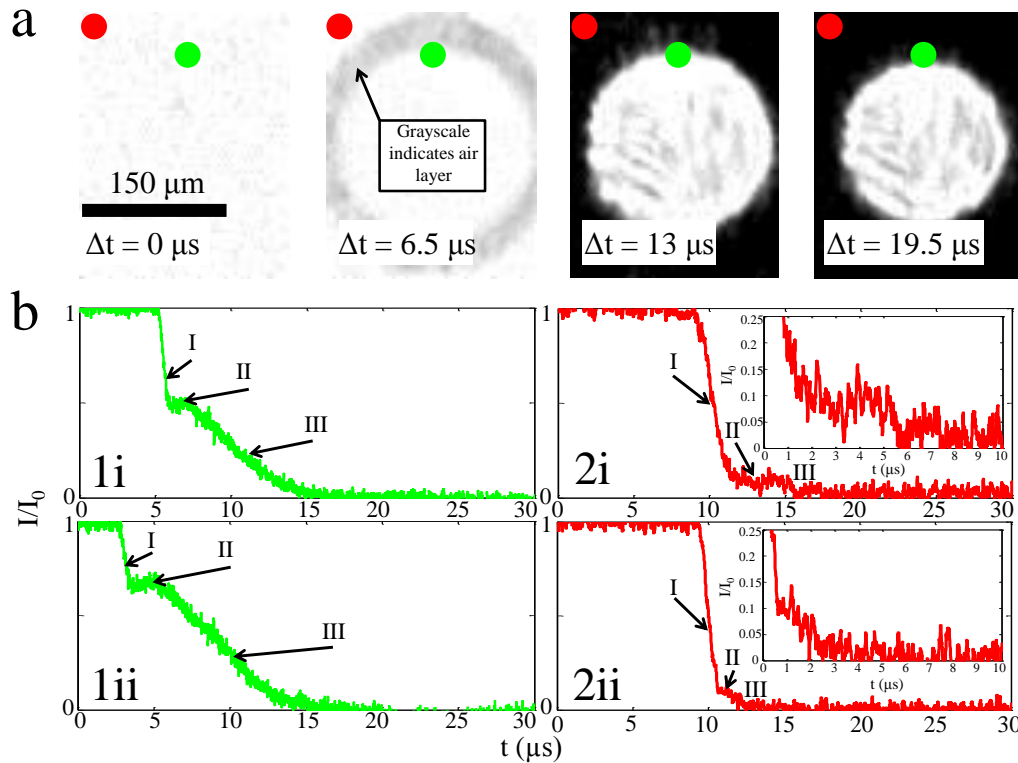


Figure A.2: (a) A sequence of images recorded at 150000 frames-per-second with one μs exposure time for $H = 21$ cm, including circles illustrating the locations probed by the photodiode: the first location, indicated by a green circle, is located partly beneath the dimple and partly beneath the initially developed air layer. The second location, shown in red, is entirely outside the immediate vicinity of the dimple. Notably, a $50\ \mu\text{m} \times 25\ \text{nm}$ air layer is directly visualized in the second frame of the image sequence. (b) The two different types of intensity traces observed for the two photodiode positions in part (a) are plotted in green and red.

plateau we find in Fig. 2.4(d) of the main text, albeit at an elevated normalized intensity, and III, the intensity slowly decreases to zero. For the second type of trace, there are again three regions: I, where the intensity rapidly drops by over an order of magnitude followed by II, a plateau where the intensity remains approximately constant for a short time before III, ultimately dropping to zero. The intensity trace plotted in Fig. 2.4(d) of the paper belongs to the second type of intensity trace.

The interpretation of the intensity traces can be interpreted in the following way: for the first type, region I corresponds to the formation of the thin film of air only partially covering the area sampled by the photodiode, immediately beneath the rim of the dimple. Due to the partial coverage of the sampling region the relative intensity drops by only a few tenths; region II corresponds to the time preceding the dewetting of this thin film of air and region III corresponds to both the rapid rupture of the air film as well as slower, inward-progressing front, which ultimately wets the area beneath the dimple. The existence of a plateau is direct evidence of the thin film of air forming beneath the impacting drop. For the second type of intensity trace, region I corresponds to the rapid (~ 40 m/s) progress of the liquid over the area sampled by the photodiode; in region II the intensity reaches a short-lived plateau above the noise level² of our signal before ultimately decreasing to zero in region III; the duration of the plateau is likely to be set by the rate of the dewetting dynamics.

²The noise level in the signal is the RMS noise of the photodiode, measured to be 1.0 mV. Since our light source maximizes intensity around 20 mV depending on the magnification used, we arrive at a noise floor of approximately 0.015 relative intensity following smoothing of the raw data by a running average with a 100 ns window.

A.4 Mathematical model

We solve for the initial radius of contact, R_0 , given by $R_0 = \sqrt{R \cdot h}$ [26], where h is the distance between the liquid and substrate when the drop is initially deformed and R is the radius of the drop. To calculate R_0 as a function of the initial drop height, H , we start from $h = R \cdot (12 \cdot \mu_g / \rho_f U R)^{2/3}$, as shown in[26], where μ_g is the gas viscosity, ρ_f is the fluid density and U is the velocity of impact, given in terms of the initial drop height by $U = \sqrt{2gH}$. Substituting the expression for h into $R_0 = \sqrt{R \cdot h}$, we obtain $R_0 = \{(R^{2/3}(12 \cdot \mu_g)^{1/3}) / (\rho_f^{1/3}(2g)^{1/6})\} \cdot H^{-1/6}$.

The speed, V , at which the fluid spreads above a thin film of air can be estimated from a simple scaling analysis. The horizontal length scale found in the previous paragraph, $R_0 \sim (R^2 \mu_g / \rho_f U)^{1/3}$, divided by the time scale of the impact, $\tau \sim (R^{1/3} \mu_g^{2/3} / \rho_f^{2/3} U^{5/3})$, as found previously by Mani et al.[27] gives a scale for the spreading velocity V to be $V = 0.34 \cdot (\rho_f R / \mu_g)^{1/3} U^{4/3} = 0.34 \cdot (\rho_f R / \mu_g)^{1/3} \cdot (2 \cdot g)^{2/3} H^{2/3}$, where the coefficient of 0.34 is determined by simulations[27]. The calculated spreading velocity agrees very well with the measured spreading velocity, as shown in Fig. 2.4(c) of the text.

Appendix B

TIR calibration methods

The implementation of TIR microscopy employed throughout this thesis is derived from a technique used to directly probe dynamics at a frictional interface[42]. Since we attempt to measure the gap thickness using the intensity, it is important to calibrate the technique. The gap thickness is calculated from the intensity as described in App. A. Using this calculation, we find that our depth of field is limited to the wavelength of the light used to probe the interface. Here, we implement two methods to calibrate the TIR technique for direct measurement of the gap thickness. In these methods, the illumination scheme used in the TIR technique is similar to the illumination scheme used in the experimental studies of droplet impact described in previous chapters of this thesis. These methods rely on comparison between the TIR measurement and a known position or trajectory in the evanescent field.

B.1 Controlled positioning of an object in the evanescent field

The TIR technique can be calibrated by controlling the position of a high-refractive index material in the evanescent field with nm-precision. Piezoelectric stages are capable of nm-precise¹ movement, and when operated in servo mode, have nm-scale repeatability. We control² the position of an object in the evanescent field using a nm-precise piezoelectric stage as shown in Fig. B.1(a) and (b). We calibrate the TIR technique by directly comparing the intensity measured beneath the object to the height measured by the piezo controller, the result of which is shown in Fig. B.1(c).

B.2 Synchronized measurement of a known trajectory using an alternative measurement modality

The TIR method can also be calibrated by synchronized measurement of the trajectory of an object moving normal to the surface³. Thus, the TIR signal can be directly compared to a known reference.

¹We use e.g. physikinstrumente P-721

²We use physikinstrumente E-665 in servo mode with strain gauge feedback. This controller includes an output voltage proportional to measured position of the piezo stage.

³A corollary method uses a spatially varying reference geometry $z_{ref}(x, y)$ such as a spherical lens for calibration of δ . First, a normalized height is calculated $z/\delta = -\log(1 - I/I_0)$. Next, δ is calibrated from this function by maximizing agreement between $\delta \times z(x, y)$ and the known $z_{ref}(x, y)$; however, unless $z_{ref}(x, y)$ is directly measured, the calibration must account for deformation at the contact zone.

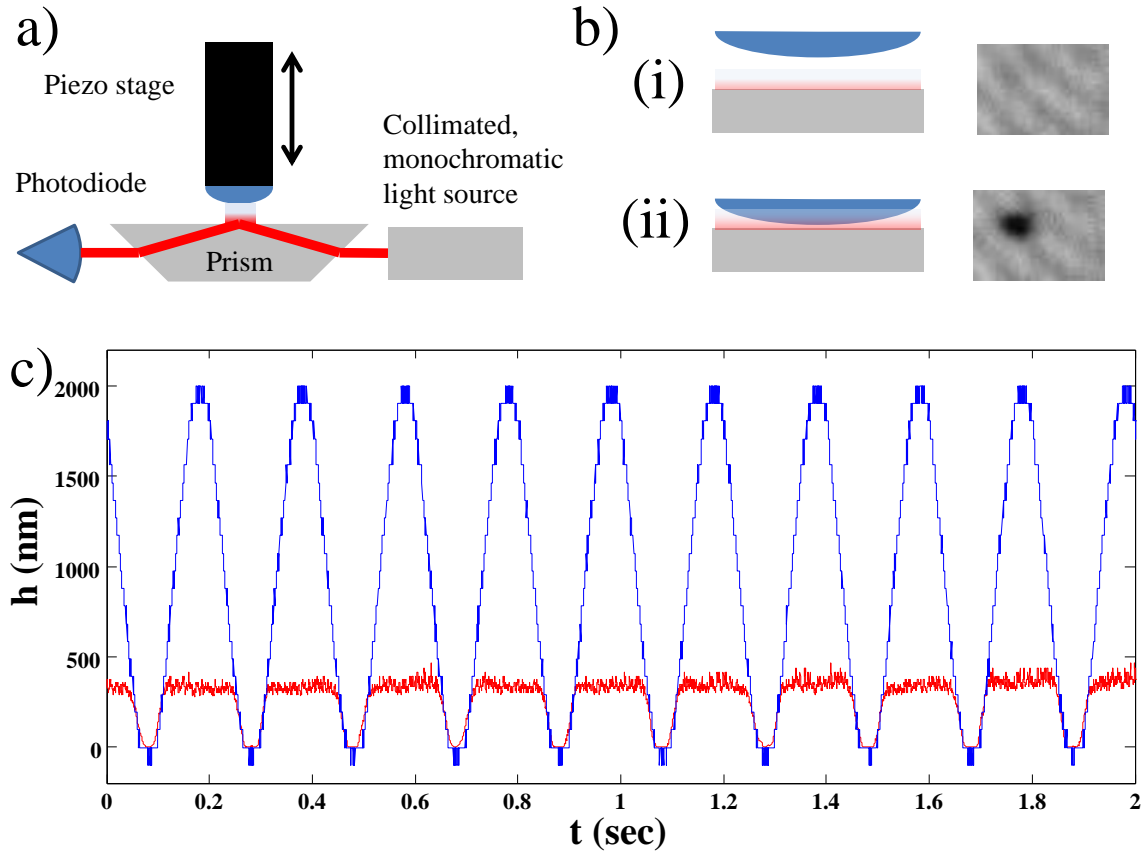


Figure B.1: Controlled positioning of a lens in the evanescent field using a piezoelectric stage in servo mode. (a) Experimental schematic, including optics and piezo stage. (b) (i) When the lens mounted at the head of the piezo actuator is at the peak of its distance from the surface of the prism, the image doesn't show any signal, as can be seen in the corresponding image to the right. (ii) When the lens is in contact with the surface, the lens appears as dark disk centered upon the solid-solid contact zone, with a gradient of intensity toward the boundary. (c) A time trace stage position (blue) is plotted with the height measured by the photodiode in red. The piezo is driven with a 5 Hz sine wave. When the lens enters the evanescent field, the height decreases in exact correspondence with the servo signal.

For this calibration, we measure the gap between the prism surface and a piece of glass using the TIR method and a Fizeau interferometer at a single point using the set-up illustrated in Fig. B.2(a); example images are shown in (b). We then remove the glass from the evanescent field; thus, we have a dynamically varying signal that we measure using these two optical methods, as shown in the graph in Fig. B.2(c). The interferometry signal is comprised of Fizeau fringes, and thus peak-to-peak intensity variations correspond to $\lambda/2$ distances, and trough-to-peak intensity changes correspond to $\lambda/4$. Direct comparison of the signals allows us to calibrate the TIR signal; using green light $\lambda = 532nm$, we find $\delta = \frac{532 \text{ nm} / 4}{z/\delta|_{peak} - z/\delta|_{trough}} = 170nm$. Since the measured position must agree at each time, we can plot the trajectory measured with the two techniques, and the trajectory matches nearly identically for the two independent measurement methods, as can be seen in Fig. B.2(d).

Both implementations of calibration methods confirm that $z = -\delta \log(1 - I/I_0)$, where $\delta = \frac{\lambda}{4\pi} \frac{1}{\sqrt{n_1^2 \sin^2 \theta_1 - n_2^2}}$.

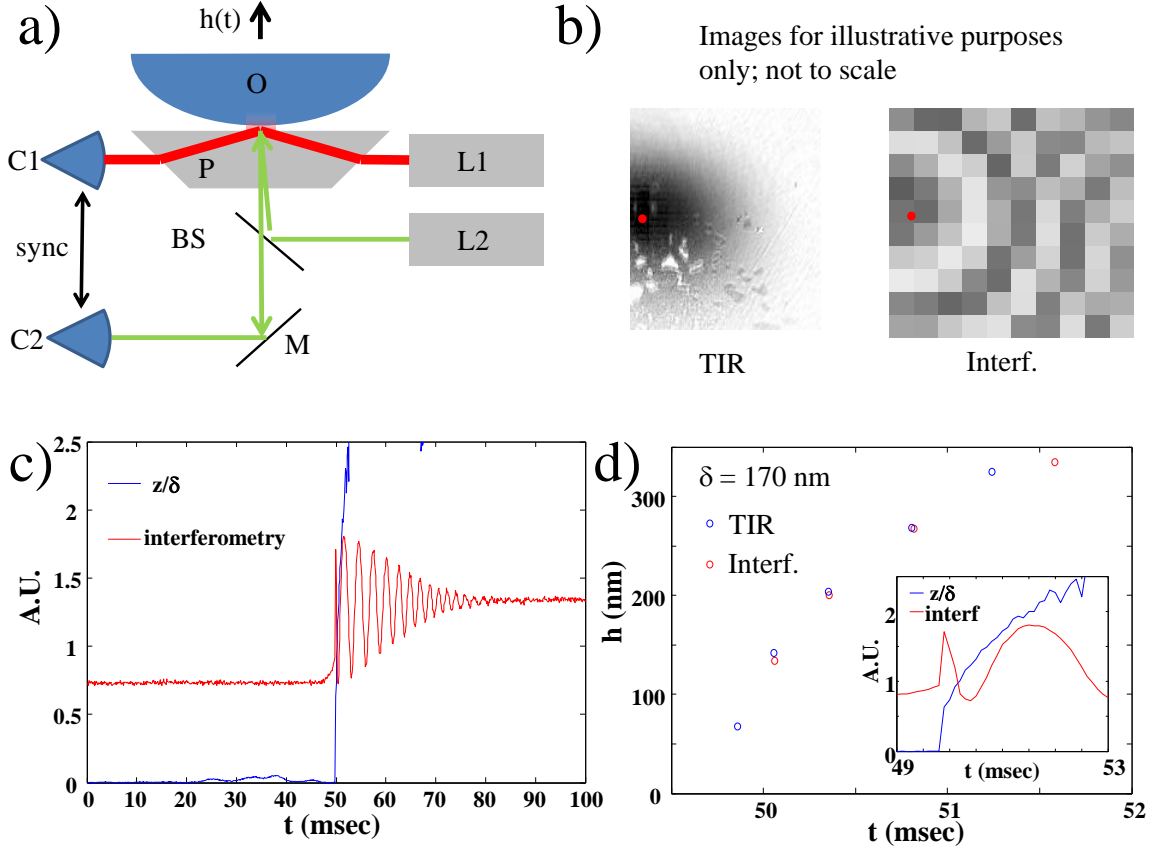


Figure B.2: Time varying signal measured using two independent optical techniques; one TIR, the other Fizeau interferometry. (a) Experimental schematic, including optics for TIR and Fizeau interferometry method. (b) Two example images: first using the TIR method, second using Fizeau interferometry. These images are not to scale, but merely illustrate that two images taken in such a manner can be correlated with one another so as to use Fizeau interferometry to calibrate the TIR method. (c) A time trace from the point corresponding to the closest approach as the glass rapidly separates from the surface at $t \sim 50$ msec. $z/\delta = -\log(1 - I/I_0)$ (d) After calibrating, the corresponding heights for a series of several points using the calibrated decay length and the TIR data (blue circles) and the interferometry data (red circles). These points agree well, indicating that the TIR technique functions as predicted by the calculation method.

Appendix C

The initiation of contact and the stability of the air film

Before a liquid drop can contact a smooth solid surface, it must drain the air beneath it. During the impact process, some of the air remains trapped, and separates the liquid from the solid. Depending on the impact parameters, this thin film of air separating the liquid from the solid can become extremely thin[26, 19]: indeed, the film thickness can approach the scale at which intermolecular forces such as van der Waals attraction become relevant[17]. While our daily experience suggests that the initiation of contact between the drop and the surface is trivial, the drop must first pierce the air before liquid-solid contact can occur; thus contact is a topological transition. Indeed, as described in Ch. 4, for sufficiently low impact velocities, the liquid will fail to pierce the thin film of air, and instead retract, thus completely rebounding from the surface.

C.1 Structure and hydrodynamics of the thin film of air

During the impact event, the liquid skates over the air, and increases the lateral extent of the film of air. The air proceeds to drain until rebound occurs, as can be seen in the kymograph of Fig. C.1 (a). A height trace taken at a radial distance of $\sim 350\mu\text{m}$ from the impact center shows two essential stages to the formation of the thin film of air separating the liquid from the solid, as shown in Fig. C.1 (b): first, the liquid rapidly approaches the surface, entraining the air at the leading edge of the drop as the liquid deforms; next, the air slowly drains from this thin gap as the lateral extent of the thin film of air increases, shown in detail inset in Fig. C.1. This behavior suggests that the hydrodynamic processes in both the liquid and the air are slow once the film of air is entrained beneath the impacting drop, and the established linear stability analysis of a thin viscous film seemingly contains all of the relevant physics[58, 62, 11]. Indeed, at the very initial stages of the development of liquid-solid contact, the length scales are necessarily very small, and both liquid and gas inertia can be neglected. Since our experiments focus on a regime of droplet impact where the liquid is strongly attracted to the solid and thus wets the solid, the interfacial attraction of the liquid to the solid is of the correct sign to destabilize the thin film of air[58, 62, 37, 11, 19].

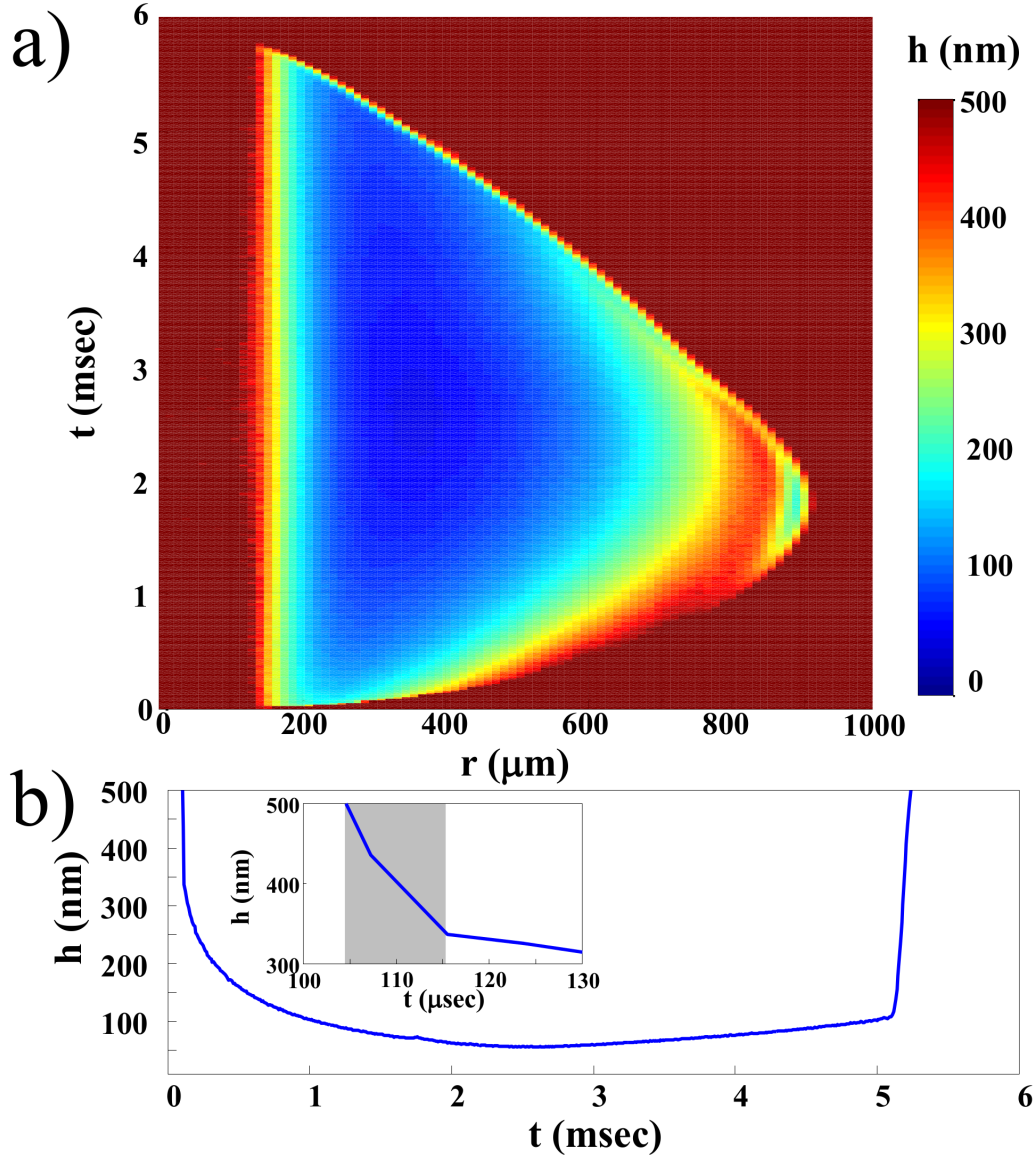


Figure C.1: Characteristic behavior of the air film during a typical rebound of a $R = 800\mu\text{m}$ drop of 10 cSt water glycerol falling at $V = 0.55\text{m/sec}$. (a) An r - t kymograph shows the spreading and retraction of the liquid drop from the air layer, which never gets closer than 50 nm from the surface. (b) The time trace taken at the point of minimal approach shows two fundamental stages in the dynamics: first, the liquid skates rapidly approaches to within 350 nm of the surface; then, the air slowly drains as the liquid continues to approach the surface. The first stage is indicated by the gray box in the detail, inset.

C.2 Linear stability analysis of thin viscous films

The linear stability analysis of such a thin viscous film suggests that interfacial forces between the liquid and the solid become relevant when the gap is smaller than 100 nm[17]. For such a thin gap, the air film becomes unstable when interfacial stresses become comparable to forces due to surface tension. The timescale required for amplification of capillary disturbances of wavenumber k on the surface of the liquid-air interface is[62]:

$$\frac{1}{\tau} = \frac{h_0^3}{3\mu_g} \left(\gamma k^4 + \frac{Ak^2}{2\pi h_0^4} \right).$$

If $\tau < 0$, any disturbance on the liquid-air surface grows; thus, the sign of the term in the brackets provides a boundary for when we expect the film to be unstable. The critical wavenumber as a function of film thickness is

$$k_0 = \sqrt{\frac{A}{2\pi\gamma h_0^4}}.$$

The values of k_0 are inversely related to the corresponding wavelength, as shown in Fig. C.2(a). The points demarcate the boundary between stable and unstable films; the unstable region is indicated in gray.

By substituting our experimental parameters¹ in to the dispersion relation, we can calculate the characteristic timescale for spinodal decomposition for a film of a given thickness. To see whether the instability develops rapidly enough to be commensurate with typical experimental timescales of 1 msec, we calculate τ as a function of k for different values of h_0 , as shown in Fig. C.2 (b). The linear stability analysis suggests that films 100 nm thick remains linearly stable, while films 10 nm

¹typical experimental values are $h_0 = 1 - 1000$ nm, $\mu_g = 2 \times 10^{-5}$ Pa.s, $\gamma = 0.07$ Pa.m, and $A = -10^{-19}$ J.

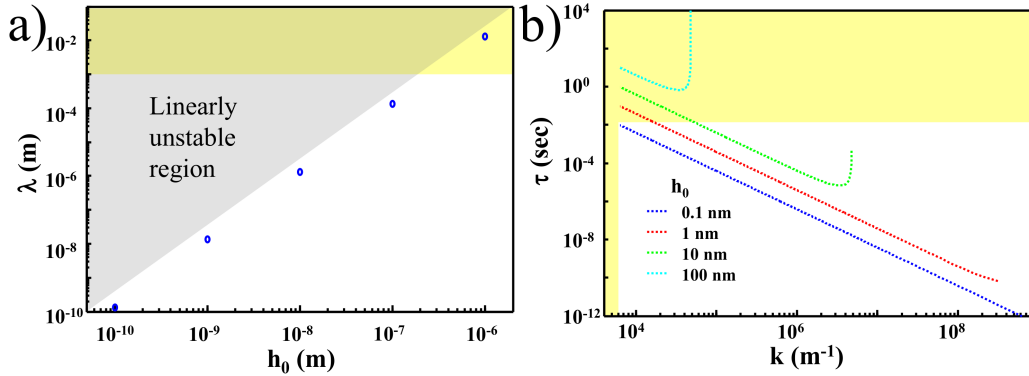


Figure C.2: Results of linear stability analysis. (a) The critical wavelength $\lambda = 2\pi/k_0$ at which the thin film becomes unstable increases with increasing film thickness. The linearly unstable region is indicated by the gray triangle; the yellow area is experimentally inaccessible because the extent of the air film beneath the liquid drop never exceeds mm-scales. (b) The timescale required to develop the instability decreases with decreasing film thickness; in parallel, the fastest growing mode shifts to higher k (lower λ) as film thickness decreases. The yellow regions are experimentally inaccessible, because the timescale required for developing the instability in the upper region of the graph is longer than the duration of the impact event for rebounding drops, and thus, while the film is linearly unstable in the region, the instability takes longer to develop than the time required for the drop to rebound from the surface.

thin can become linearly unstable, and films thinner than 10 nm will rapidly dewett the surface. This trend is consistent with our experiments, as discussed in Chs. 2 and 4; however, for all experiments conducted on atomically smooth surfaces, we do not observe liquid solid contact for a film of greater thickness than ~ 5 nm in the absence of nucleation. Indeed, contact initiates suddenly from a measurable height above the surface; independent of how the air film is formed, we consistently measure a film thickness of ~ 1.5 nm immediately before contact initiates, and therefore refer to this height as a critical height h_c at which contact initiates, as described in Ch. 4. This is in striking contrast to the prediction of the linear stability analysis, which says that a 1.5 nm thin film of air will dewett the surface in 0.5 nsec, with a characteristic wave number $k_c = 1.6 \times 10^8 \text{m}^{-1} \rightarrow \lambda_c = 40$ nm; λ_c is well within the maximal extent of the air film beneath the drop.

C.3 Time duration of air film before initiation of liquid-solid contact

The impact of droplets on glass motivated the argument for a spinodal-like dewetting mechanism for contact. However, the increasing rate of liquid-solid contact initiation as film thickness decreases is also consistent with nucleation driven contact; in particular, many of the contacts we observed formed from distances exceeding 100 nm from the surface. Contact events from similar heights were measured in a study of the breakdown of the air film beneath an impacting drop by de Ruiter et.al.[12]. We recorded the height-time traces for all points where liquid-solid contact initiated

$x^*(i)$. We measured the time dt between first-passage of the liquid above $x^*(i)$ and the initiation of contact; simultaneously, we measured the height $h^*(i)$ immediately prior to contact formation. These data allow for direct comparison between the timescale predicted by linear stability analysis for spinodal dewetting of the air film and the measured dt , shown in Fig. C.3. The majority of the data fall outside of the region where the air film is predicted to be linearly unstable. Since the measured dt are less than the values of τ calculated from the linear stability analysis, nucleation events are likely responsible for the initiation of liquid-solid contact in these cases.

Surface profilometry will reveal the presence of nucleation sites on the glass surface; however, direct observation of the glass surface with lateral resolution on the nm-scale is not possible using traditional optical techniques. Instead, nm-scale lateral resolution requires an AFM. We analyzed the surface profiles of our freshly cleaned microscope slides², and found that the glass slides are very smooth on average. However, a randomly selected $50 \mu\text{m} \times 50 \mu\text{m}$ region of interest contained several peaks as high as 20 nm; such peaks demonstrate the presence of nucleation sites for liquid-solid contact on glass surfaces at a height scale comparable to the air film thicknesses beneath the impacting drop, and these nucleation sites can cause the disruption of an otherwise linearly-stable thin film of air.

The initiation of liquid-solid contact on glass surfaces occurs more rapidly than the timescale for development of an instability; in contrast, the initiation of liquid-solid contact on atomically smooth mica occurs long after the thin film of air should have become unstable. Thus, it appears as though additional dynamics stabilize the

²We are grateful to Sidney Cohen at the Weizmann Institute of Science for assisting us with the AFM

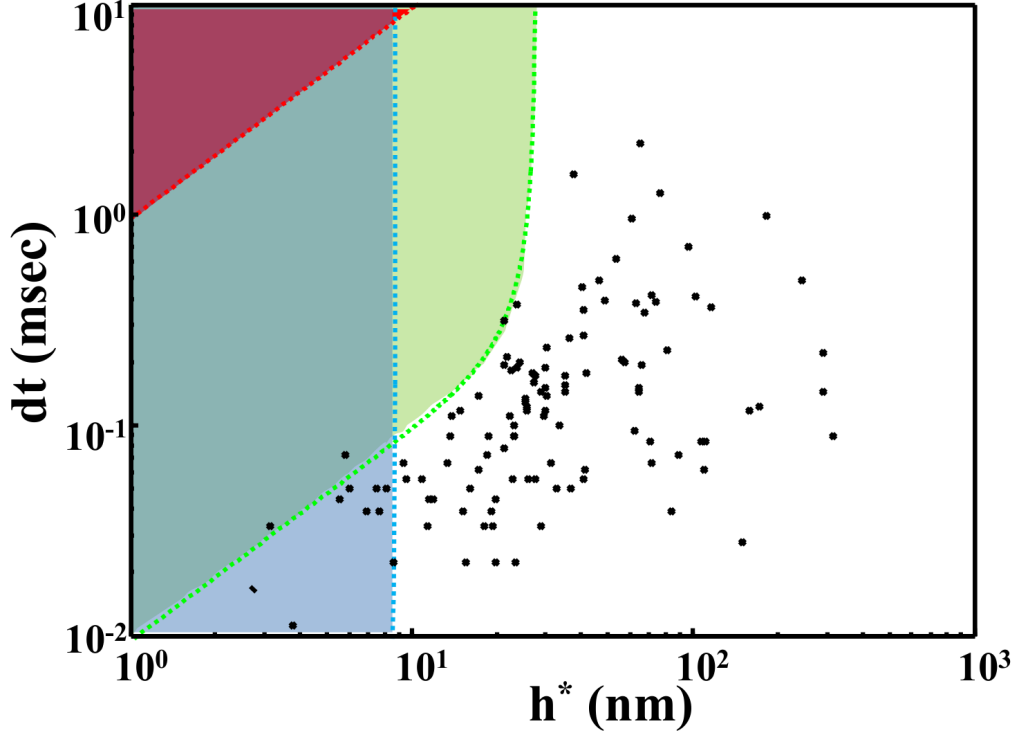


Figure C.3: Timescale for the development of linear instability of a thin film of air. The data comprise an ensemble of $dt-h^*$ pairs measured immediately before the initiation of contact for over 40 impact events over a range of V . In almost the entire plot, the data fall on an unshaded region of the graph. The unshaded region is the region for which the dt and h^* combination are linearly stable for all k . With the exception of the smallest value of k , none of the observed contact initiation events occurred when the film was linearly unstable. The three shaded regions correspond to values of dt at which a film of the corresponding thickness is linearly unstable; the three colors (red, upper left; green, center; blue, at left) correspond to $k = 2\pi \times 10^4$, $2\pi \times 10^5$ and $2\pi \times 10^6$, respectively.

thin film of air, and occlude the formation of contact.

C.4 Initiation of contact on atomically smooth mica

A representative time-series of images recording the initial stages as the liquid contacts the solid beneath an impacting drop is shown in Fig. 4.4(a). While the distribution of contacts always occurs on the circumference of a well-defined ring of contact, the distribution of contacts about the ring is not identical for all V . In order to compare the distribution of contacts around the ring for different V , we measure $h(t)$ on the circumference of the ring of contact, centered on the impact axis, with radius $r_r = \langle r_i^* \rangle$ where r_i^* is the radial distance from the impact axis to the point at which contact i initiates, as indicated schematically in the inset of Fig. C.4 (a). Thus, we ‘unwrap’ the ring of contact formation, and make a kymograph in $\theta-t$ as shown in Fig. C.4 (a). For drops impacting with $V = 0.84$ m/sec, fewer contacts form at greater mutual separation than the number of contacts forming beneath drops impacting with $V = 0.95$ m/sec, as can be seen in the kymograph in Fig. C.4 (b). dt will decrease as V increases because the height at which the air film initially forms decreases with increasing V . However, h_c is constant as V varies; thus, we might anticipate that the standard deviation of contact initiation times σ_{dt} would also be independent of V . However, This intuition is misleading, because the standard deviation dt falls off sharply with V , as can be seen in Fig. C.5. While the hydrodynamics of the formation of the thin film of air play no role in determining the thickness from which the thin film of air ultimately ruptures, they affect the collective rupture dynamics.

The air layer remains stable long past when it should have become linearly unsta-

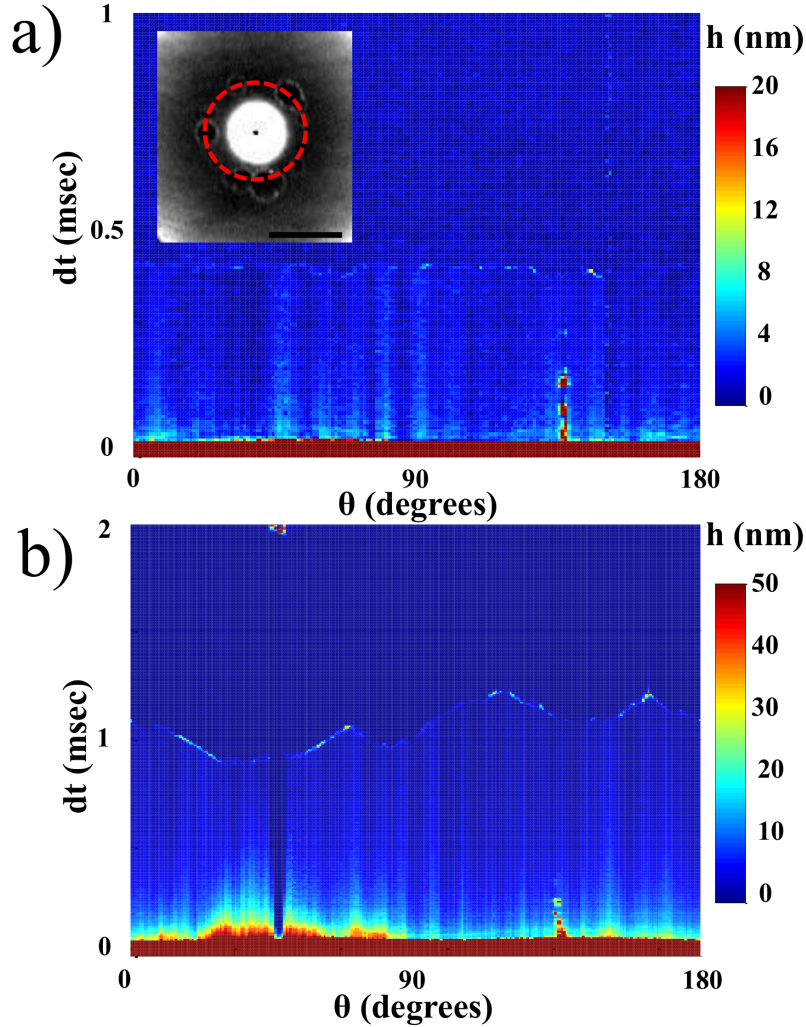


Figure C.4: Kymographs of the initiation of contact about the ring of contact. (a) For impact velocities approaching 1 m/sec, the liquid initiates contact about the ring of contact with a well-defined spacing between the contacts, as can be seen in the snapshot inset. The red dashed circle represents the circle of contact schematically. Contacts suddenly initiate shortly before 0.5 msec have transpired; the dark blue region from 0.5 msec to 1 msec, the liquid is in contact with the solid. The low-contrast is caused by the real physical proximity of the liquid to the solid before contact initiates. Here, red represents 20 nm or higher; the liquid continues to approach the surface for nearly 0.5 msec from an initial height of approximately 10 nm. (b) For $V = 0.84$ m/sec, the air film requires nearly twice as long to drain to h_c ; furthermore, the time required to completely close the circle of contact is far longer. The circle of contact requires nearly 0.25 msec to close once the first contact initiates at approximately 1 msec.

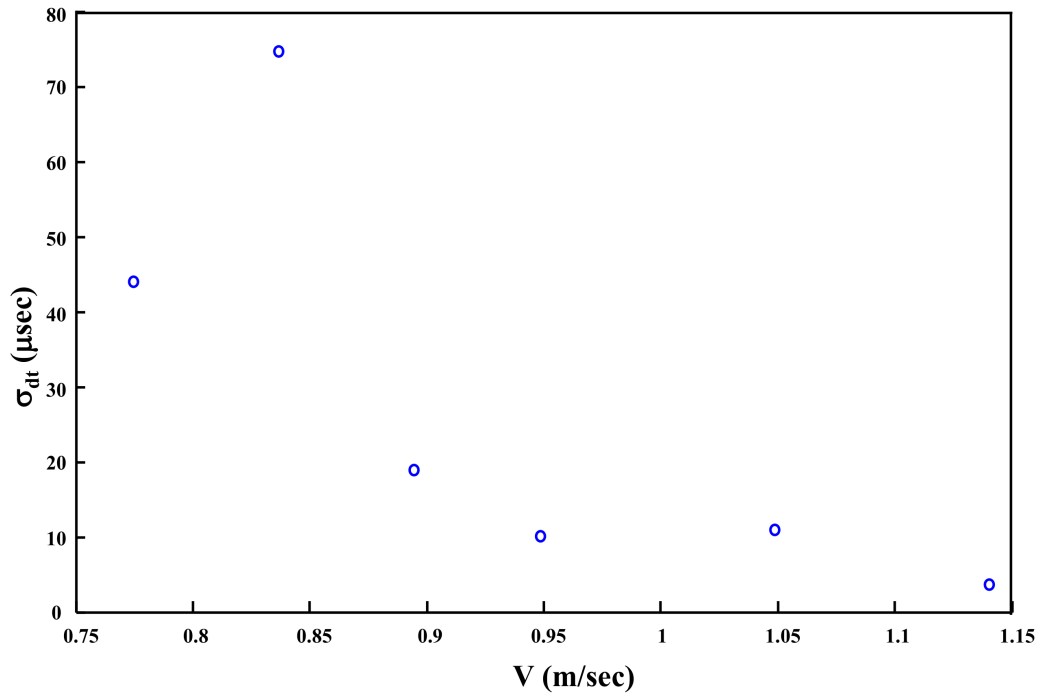


Figure C.5: The standard deviation of dt generally decreases as V increases, with an exception for $V = 0.85$ m/sec. The decrease of the σ_{dt} as V increases implies that the contacts are not forming independently; they are influenced when a neighboring point on the circle of contact has made contact with the surface.

ble, suggesting that the linear stability calculation does not contain all of the physics governing the initiation of contact between a liquid drop and an atomically smooth, hydrophilic surface through a nm-scale layer of air.

Appendix D

The propagation of liquid-solid contact through thin air

The dynamics the three-phase contact line are relevant to many industrial processes, and are ubiquitous in our daily experience; in spite of this ubiquity, there are important aspects of liquid-solid contact line dynamics that remain poorly understood. A particularly striking instance of liquid-solid contact occurs beneath an impacting drop. Prior to the formation of contact, the drop will skate laterally outward over a thin film of air; subsequently, liquid-solid contact initiates at a point beneath the liquid[19]. The air is of critical importance in the splashing phenomenon[65]. Numerical and analytical models suggest that the air provides a mechanism for a splash[26, 27, 25]. This formation of contact through the thin film of air is ostensibly similar to the initiation of contact beneath a liquid drop as it is brought slowly toward a surface; however, the mathematical models describing these dynamics ignore the surrounding air[3, 4, 10]. Simulations show that the surrounding air indeed influences

the dynamics of droplet coalescence[2], which is an analogous problem; however, experimental data, and a corresponding theoretical framework describing the dynamics of liquid-solid contact in the presence of such a thin film of air is absent from the literature.

Using TIR microscopy[42, 19], we directly probe the dynamics as liquid-solid contact develops through a thin film of air beneath an impacting drop. The experimental set-up is shown in Fig. D.1(a). This technique allows us to record the three-dimensional shape of the liquid-air interface once contact initiates, as shown in Fig. D.1 (b) and (c). We alter the liquid parameters to explore the phase-space of liquid-solid contact on a surface of smooth glass. To form the thin film of air, we release drops onto the surface from various heights[19]. We take advantage of inherent asperities on the glass surface to nucleate contact through thin films of air from various distances from the surface.

D.1 Initiation of liquid-solid contact at a point

Liquid-solid contact initiates at a point for each viscosity and film thickness we measured; the time-series of images of an example contact event for 10cSt water glycerol solution is shown in Fig. D.2(a). After liquid-solid contact initiates, a wetting front begins to spread laterally outward at a constant velocity that depends on the liquid viscosity; the shape of the profile, however, consists of the same fundamental features for all air film thicknesses and all liquid viscosities: the spreading contact is surrounded by what appears as a ‘halo’ in images. This ‘halo’ region at the leading edge of the contact appears to contain the air as it is displaced by the wetting liquid.

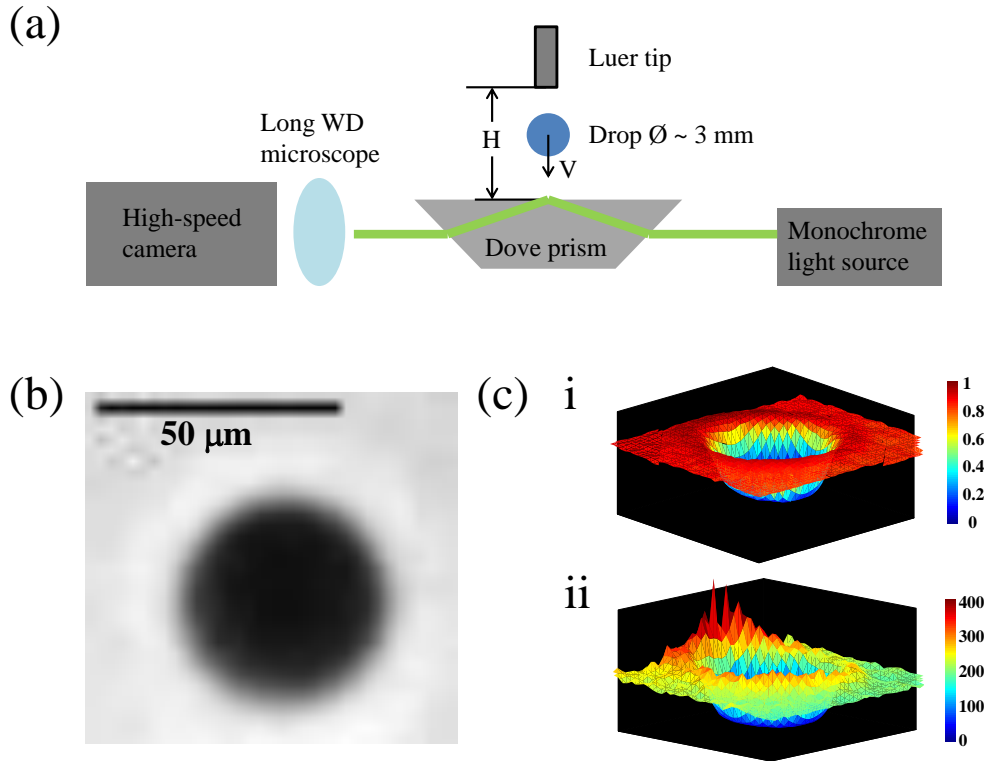


Figure D.1: (a) Schematic layout of optical components for TIR microscopy. Collimated, monochromatic light enters a dove prism such that it totally internally reflects off of the glass-air interface, exciting an exponentially decaying evanescent wave at the surface; the incidence angle is tuned such that the light transmits through a glass-liquid interface. We image the light on our camera's sensor after it exits the prism. (b) A sample image of a contact patch is shown, where grayscale is a measurement of the height of the liquid above the solid surface. (c) We convert from intensity in (i) to height in (ii), as shown.

As the wetting front displaces the air, the air cannot drain immediately, and will not compress infinitely; thus it pushes the liquid up and away from the surface.

To probe these dynamics, we plot kymographs of the liquid-air profile, which record the radial position of the contact as a function of time. These kymographs show that the wetting front moves more slowly for liquids of higher viscosity, as shown in Fig. D.2 (b)-(d). Contact initiates at $t = 0$, $r = 0$. From this point, we see a triangular wedge of dark blue, which indicates the radial growth of the wetted region, in each of the experiments; this triangle is labeled ‘liquid-solid contact’ in Fig. D.2 (b). The wetting front is far from the edge of the liquid, where the air is entrained as the breadth of the air film increases. The kymographs show wetting fronts that propagate through air films of different thickness. The slope of the line at the leading edge of the triangular region indicates the propagation velocity of the front. The wetting front propagates at a strikingly different velocity for the viscosities shown; the wetting front always advances more slowly through the thin film of air for larger liquid viscosity.

D.2 Propagation of the contact line along the surface

A time-series of profiles measured as the wetting front progresses over the surface from left to right shows that the halo does indeed grow vertically away from the surface, as shown in Fig. D.3(a). The velocity of the wetting front remains nearly constant, and is independent of the thickness of the air film through which it propagates

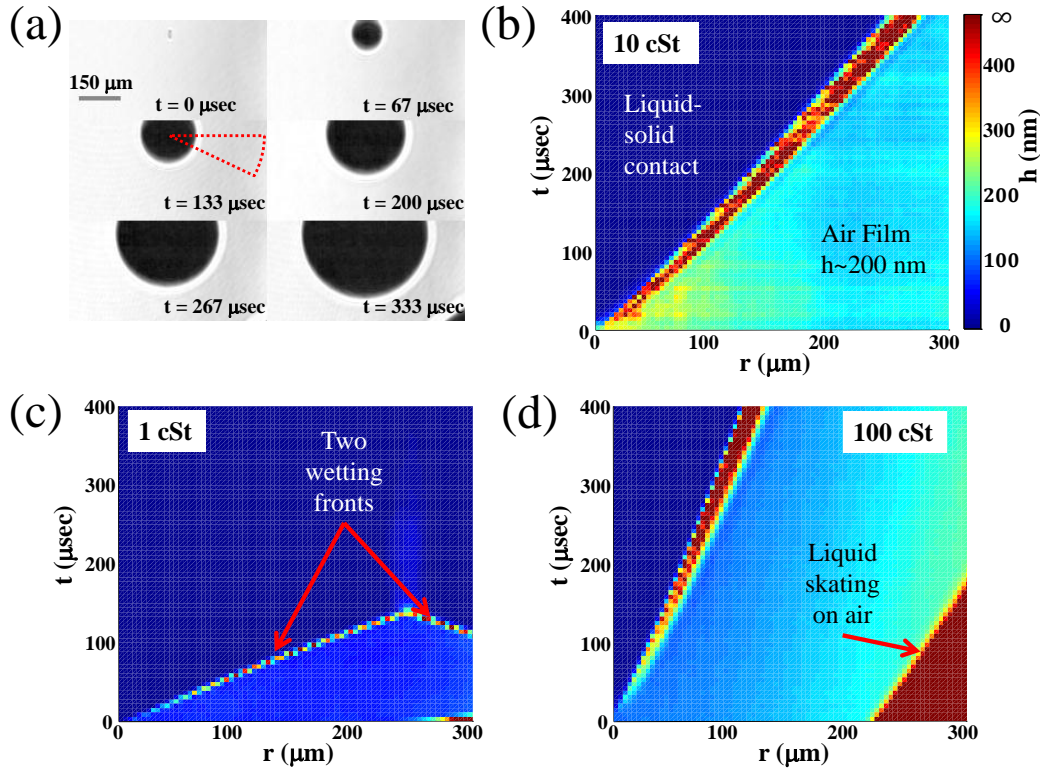


Figure D.2: (a) A series of photos of a contact forming beneath a thin layer of air between a smooth, solid surface and 10 cSt liquid. At $t = 0$, the contact forms. The contact line moves symmetrically out from the point of contact formation, and a ‘halo’ forms ahead of the contact line, where the displaced air is accumulated. (b) Traces of azimuthally-averaged height are plotted as a function of space and time for 10 cSt liquid. The contact line progresses linearly in time, indicating a constant velocity; furthermore, the size of the halo region leading the contact line grows over time. (c) A similar space-time-height plot for 1cSt liquid; here, two contact lines can be seen moving over the surface, as indicated. The contact line progresses linearly over time with a lesser slope, indicating a greater velocity. (d) A space-time-height plot for 100 cSt liquid contact line moving through a 150 nm thin film of air; here the contact line progresses linearly in time with a steeper slope, corresponding to a slower contact line velocity.

for a given liquid viscosity, as shown for 19.6 cSt liquid in Fig. D.3(b).

D.3 Characteristic geometry of the propagating contact line

At the earliest stages of contact formation and growth, we directly observe the geometry of the liquid-air interface, and measure the height dh and breadth ℓ_{halo} of the halo at the leading edge of the contact. We find that the halo initially grows both laterally and vertically. The lateral scale of the halo $\ell_{halo} \sim t^{1/3}$ for every viscosity measured, as shown in Fig. D.3 (c). Using this scaling to fit a pre-factor, we find that over a range of film thicknesses and liquid viscosities, the pre-factor is approximately the same, as shown in the inset to Fig. D.3 (c). Over the range of viscosities measured, ℓ_{halo} varies slowly while the wetting front propagates at an essentially constant velocity.

D.4 A phenomenological model for the propagating contact line

The halo can be modeled as a capillary disturbance with a wave number corresponding to the average length of $\langle \ell_{halo} \rangle_t = 20\mu m$. The velocity resulting from a balance of inertial and capillary stresses[11] is:

$$\rho c^2 = \frac{\gamma}{\ell_{halo}} \rightarrow c = \sqrt{\frac{\gamma}{\rho \ell_{halo}}}.$$

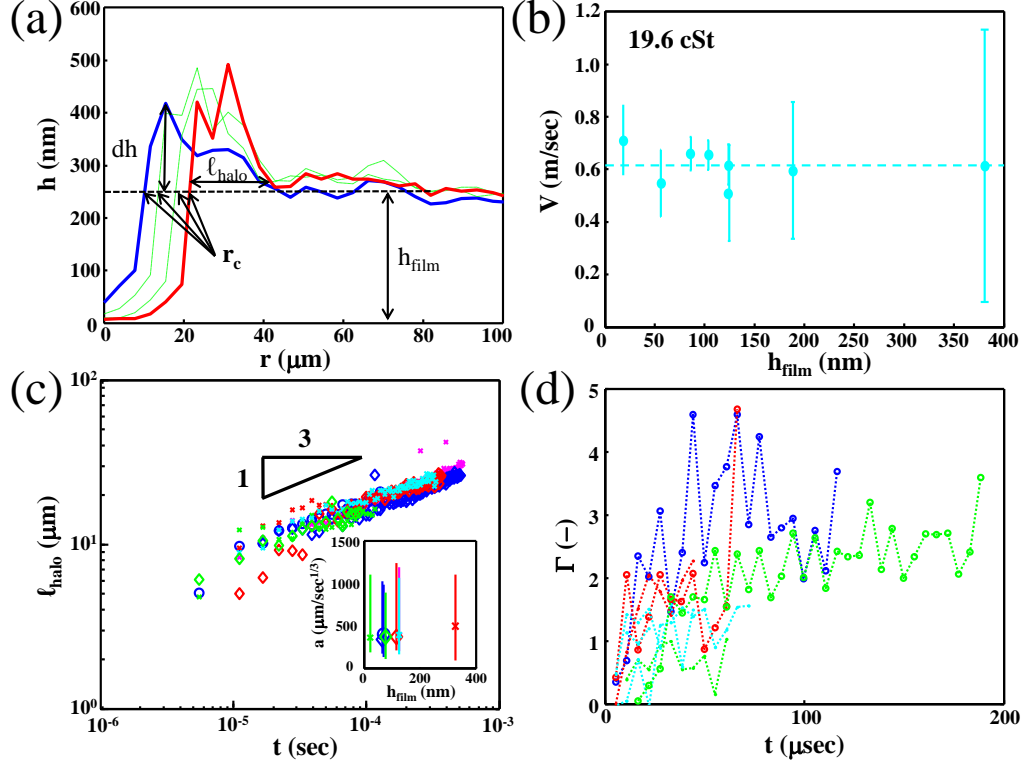


Figure D.3: (a) A time series of profiles of a contact propagating outward from the point of initiation. The propagating front excites a capillary wave at it's leading edge, which apperas as a 'halo' at the periphery of the contact in our images, with lateral dimension ℓ_{halo} and vertical extent dh . The front position is measured at the height of the film in the far field h_{film} , as indicated by the arrows. (b) The contact line velocity V in m/sec as a function of film thickness in nm for the 19.6 cSt water-glycerol solution. Here, we find that V is essentially independent of film thickness; this holds true for all viscosities measured. (c) ℓ_{halo} grows as $t^{1/3}$; this power suggests that at long times, ℓ_{halo} changes very little from a value of approximately $20 \mu\text{m}$, independent of both ν , as shown in the main figure, and h_{film} , as shown in the inset, where pre-factors of a $t^{1/3}$ fit are plotted as a function of h_{film} . (d) Γ , The ratio of the volume of air contained in the halo, $2\pi r_c \ell_{halo} dh$ to the volume of air displaced by the contact, $h_{film} \pi r_c^2$, is approximately constant in time, indicating that the air displaced by the contact is accumulating in the halo.

Substituting the average value of $\ell_{halo} = 20\mu m$ into this expression, we find that

$$c \approx 1.9m/s,$$

in qualitative agreement with the velocity of the 1 cSt water - glycerol solution, the solution with the lowest viscosity used in our experiments. This velocity is indicated by the green dashed line in Fig. D.4.

The balance of viscous and capillary stresses is:

$$\frac{\gamma}{\rho\ell_{halo}} = \nu \frac{V}{\ell_d}.$$

Substituting $\ell_d = \sqrt{\nu\tau}$, where $\tau = \frac{\langle \ell_{halo} \rangle_t}{V}$, the equation becomes:

$$\frac{\gamma}{\rho\ell_{halo}} = \sqrt{\frac{\nu}{\ell_{halo}}} V^{3/2} \rightarrow V = \left(\frac{\gamma}{\rho\sqrt{\nu\ell_{halo}}} \right)^{2/3} \rightarrow V \sim \nu^{-1/3}.$$

For our experimental parameters, $V = 0.0626\nu^{-1/3}$. This line is plotted in black squares in Fig. D.4. While this velocity agrees with the scaling of the experimental data, it requires the wetting front to exceed the capillary velocity for a disturbance equal in size to the measured values for $\langle \ell_{halo} \rangle_t = 20\mu m$; therefore, we correct this line according to the capillary wave speed when inertia is most dominant, in the low-viscosity limit. For zero viscosity, the wavespeed of such a capillary disturbance is calculated above $c \approx 1.9$ m/sec; this requires a pre-factor of approximately $1.9/6.3 \sim 0.3$ to correct for the capillary wave velocity limit corresponding to the observed disturbance. When we multiply the value calculated above by this additional pre-factor, we find $V = 0.019\nu^{-1/3}$, as plotted in the black x's in Fig. D.4. This agrees quantitatively with the data¹.

¹Here, we assume ℓ_{halo} is independent of t ; this is clearly not true, since we observe $\ell_{halo} \sim t^{1/3}$ in Fig. D.3(c). However, this results in an extremely weak dependence of $V \sim t^{-1/9}$, and thus using $\langle \ell_{halo} \rangle_t = 20\mu m$ is justified. It would be of interest to calculate why ℓ_{halo} takes this value on average.

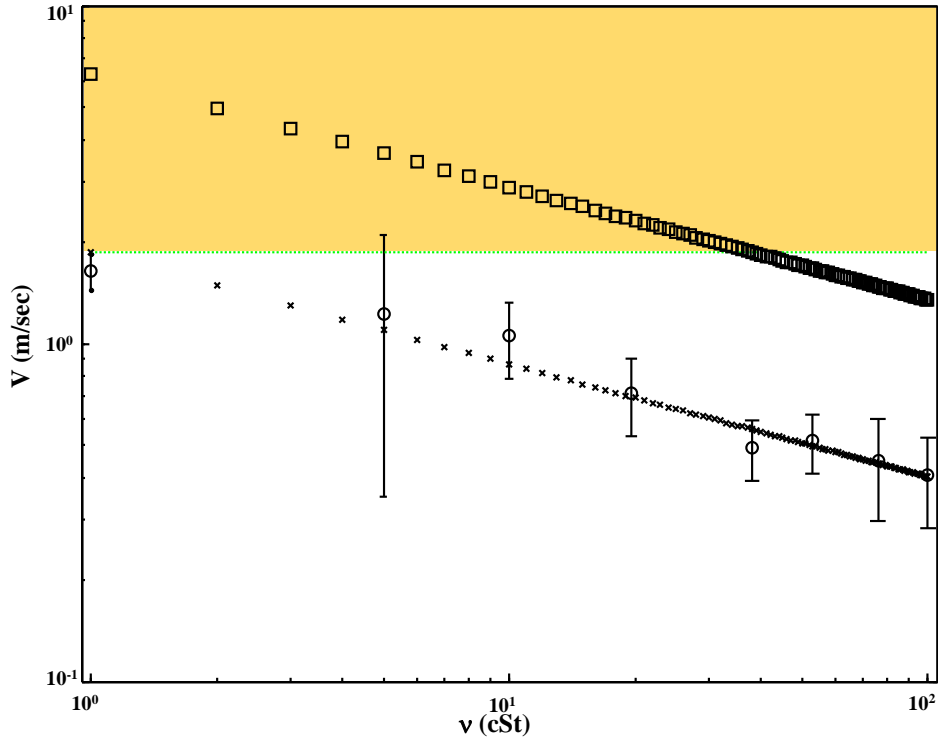


Figure D.4: The contact line velocity averaged over several contacts decreases as liquid viscosity increases; here, error bars are calculated for each viscosity from the standard deviation of all contacts measured. The average contact line velocity decreases as a non-linear function of liquid viscosity. The observed trend does not agree with $V_{cl} \sim 1/\nu$; indeed, we observe a different scaling. The green solid line shown at the top of the plot is the velocity for a capillary disturbance of wavelength $\lambda = 20\mu m$, the length at which ℓ_{halo} varies slowly in time, as can be seen in Fig. D.3(c); this velocity sets a speed limit for V_{cl} , indicated graphically by the orange shaded region. A model balancing viscous and capillary stresses as described in the text shows good agreement with the scaling of the experimental data; however, this calculated velocity exceeds the capillary wave speed, as described above; if we correct the predicted velocity by multiplying by 0.3, V_{cl} no longer exceeds this speed limit for even the least-viscous fluid used in our experiments, and the model shows qualitative agreement with the data.